Ion conduction characteristics in small diameter carbon nanotubes and their similarities to biological nanochannels

Hasti Amiri

Submitted in partial fulfillment of the
requirements for the degree
of Doctor of Philosophy
in the Graduate School of Arts and Sciences

COLUMBIA UNIVERSITY

2015

ABSTRACT

Ion conduction characteristics in small diameter carbon nanotubes and their similarities to biological nanochannels

Hasti Amiri

In this study, we designed a series of experiments to determine the factors governing ion permeation through individual carbon nanotubes (CNTs) less than 1.5 nm in diameter and 20 μm in length. We then rationalize the experimental results by using a model, which is drawn from previous literature on protein ion channels and is centered around a simplified version of the Gouy-Chapman theory of electrical double layer. Lastly, we experimentally demonstrate and discuss the general similarities in ion permeation characteristics between CNTs and biological ion-selective pores. The role of many potential factors influencing the ion transport is assessed by taking two experimental approaches: (1) studying the effect of electrolyte concentration and composition on channel conductance and reversal potential, and (2) examining a second type of nanochannel as a parallel ion conduction pathway within the same device architecture and measurement set-up, which we refer to as leakage devices. This helps to differentiate the effect of CNT on ionic transport from any other possible source. Taken together, these two experimental methods provide strong evidence that the electrostatic potential arising from ionized carboxyl groups at the nanopore entrance has a significant effect on ionic permeation in a manner consistent with a simple electrostatic mechanism.

Table of Contents

Nanofluidics Transport: Principles and Applications

Single-Nanotube Electrophysiological Measurement Platform

Ion Conduction in Carbon Nanotubes: Selectivity and Permeability

Effect of Pore Surface Charges on Ion Conduction through Carbon Nanotubes

Conclusion and Outlook

List of Figures

List of Tables

Acknowledgments

First, I would like to extend my gratitude to my advisor, Professor Colin Nuckolls, for his guidance and support during my years of study at Columbia University. Colin is a brilliant scientist with profound knowledge and keen insight into the fields of chemistry and materials science.

Second, I would like to extend my special thanks to Professor Ken Shepard, with whom I worked closely in the last three years of my PhD studies. Ken is an outstanding, fearless and hard-working researcher who constantly expands and deepens his knowledge and research horizons. He always took the time out of his busy schedule to discuss my project with me in detail, gave me invaluable feedback and encouraged me to carry on whenever I encountered an obstacle in my research. One special memory of Ken that I will always remember is when he told me he had started reading a biology book, way outside of his field of research, purely because I was reading it and he wanted to be able to discuss my preliminary results with me. I think this speaks to the type of person Ken is – his intellectual capacity and curiosity is simply astounding. He taught me that no matter how advanced and knowledgeable you are you should never seize to learn new things. I am very grateful for the opportunity Ken has given me to pursue my PhD under his guidance. Besides Colin and Ken, I would also like to thank my other thesis committee members, Dr. Mike Steigerwald, Professor Louis Brus and Professor Ruben Gonzalez, for taking the time to read my dissertation and serve in my dissertation committee. I feel extremely fortunate to come across all these great scientists during my time at Columbia University.

I would also like to thank all of the students and post-docs who I had the pleasure to get to know and work with in the past five years. I am truly thankful to all members of the Nuckolls lab, both present and past, for always being helpful, kind and pleasant to be around. I wish each and every one of them a great life and career ahead. I would like to extend my gratitude to Professor Haitao Liu, a former post-doc from whom I inherited this project. During my first year, he taught me a great deal regarding the physics of solid-state devices and their fabrication techniques. Haitao generously helped me to get on my feet, and I am very fortunate we were able to work together. I would also like to thank Dr. Bumjung (James) Kim who was always my ”go-to” person in the lab. His patience, knowledge and assistance were a great asset to me during my studies.

In the past three years, I was fortunate enough to collaborate and work closely with many members of the Shepard group. I would like to particularly extend my deepest gratitude to Steven Warren, Professor Jacob Rosenstein, Charishma Puliyanda, Scott Trocchia, Jared Roseman and Dr. David Tsai; you were all great colleagues and continue to be great friends.

I would like to thank our present and former cleanroom and shared facility staff at Columbia University - particularly Geoff Goold, for his hard work and effort to maintain the operations of the shared facilities. I would also like to mention and thank our group coordinators over the years - Mike Ewing, K.O Campbell and Liz Powell - as well as our chemistry department staff - Alix Lamia and Dani Farrell - for always being responsible and organized, helping us students to worry only about research.

My deepest love and thanks goes to my greatest treasures in life, my friends and family. Words can never express how grateful I am to my beloved father, Kazem, for devoting his life to my happiness and success; my dear sister, Shadi, for always having my back in life and my late mother, Sheida, who I miss everyday. I would like to take this opportunity to also thank a few of my dear friends, as I greatly benefited from their love, advice and encouragement during my graduate studies. I am deeply thankful to Professor Shadi Shahedipour for being a great mentor and friend to me throughout these years, Dr. Ardavan Zandiatashbar for being the best friend anyone could ever wish for and Dr. Paolomi Merchant for riding the graduate school roller coaster with me and holding my hand through all the ups and downs.

Finally, what made this journey all worthwhile was meeting my fiancé, William O'Connell. His selfless love, kindness and constant support gave me the strength and courage to get through the more difficult moments of graduate school. I am deeply grateful to him for being so generously understanding and accommodating. Detailed editing of my dissertation is perhaps among the smallest things he did for me in our years together. I would also like to sincerely thank his family for all of the love, support, Italian food and funny jokes they sent my way.

In dedication to:

my beloved father, Kazem, my dear sister, Shadi, and my late mother, Sheida

the love of my life, William

and all of the dreamers in Iran

CHAPTER 1

Nanofluidic Transport

Principles and Applications

1.1. Introduction

Nanofluidics is the study and application of fluid transport through confined structures with at least one characteristic dimension below 100 nm [1]. Over the past decade, nanofluidics has been gaining momentum as an independent discipline due to the significant development in fabrication techniques and its relevance in technological and biological applications [2].

One of the major outcomes of studying the transport phenomena in nanoscale and understanding the relationship between structure and function of nanopores was the emergence of a powerful technique for label-free and real-time detection and analysis of single molecules [3, 4]. One of the key tenets of nanopore technology is that small nanopores can act as molecular Coulter counter devices [5]. Information in this approach is often extracted from modulations in ionic current as individual molecules are electrophoretically driven through a nano-sized hole in a supporting membrane separating two aqueous reservoirs [3].

The first report of single-molecular detection using a nanopore was done by Kasianowicz et al. in 1996, where translocation of single biomolecules through a single bacterial α-hemolysin channel in a lipid membrane caused a detectable change in ionic current passing through the nanopore (Fig. 1.1) [6].

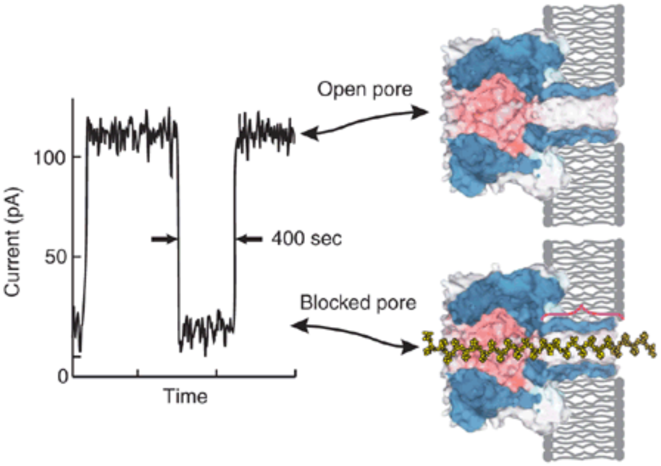

Figure 1.1 Blockade of ionic current flowing through a single Staphylococcus aureus α-hemolysin pore in a lipid bilayer membrane as individual molecules translocate through the pore [6]. Right: illustration of the process. Left: the signal caused by single analyte molecule translocation. Adapted in part from ref. [7]

Over the past two decades, various biological pore-forming proteins such as α-hemolysin ion channel embedded in a lipid bilayer [6] and synthetic nanopores fabricated by etching small holes into thin synthetic substrates such as silicon nitride [8] have been employed in nanopore-based research. Figure 1.2 shows a few examples of different types of biological and synthetic nanopores. The majority of these studies were performed with the goal of ultra-fast DNA-sequencing. Figure 1.3 illustrates proposed measurement concepts for DNA sequencing in nanopores.

Recently, it has been shown that translocation of individual nucleoside monophosphate molecules of different type causes a distinct reduction in ionic current through aminocyclodextrin-modified α-hemolysin [9]. The results of this study place nanopores among the highly promising technologies for rapid sequencing of DNA.

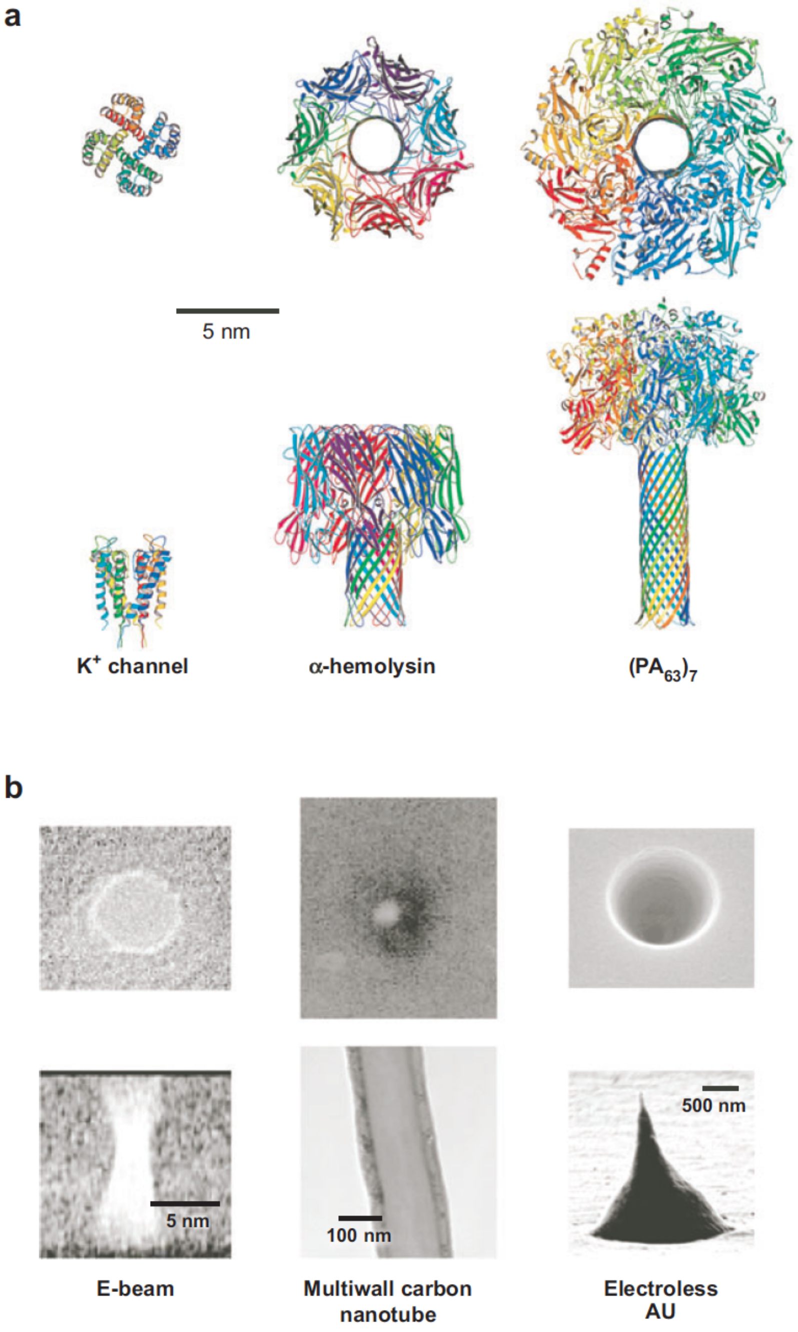

Figure 1.2 Top and cross-sectional view of biological and synthetic nanopores. a) Biological nanopores. From left to right: Potassium ion channel [10], Staphylococcus aureus α-hemolysin [11] and Bacillus anthracis protective antigen 63 $(PA_{63})_7$ [12]. b)

Synthetic nanopores. From left to right: Nanopore created in a thin membrane of silicon nitride [13], multi-walled carbon nanotube (MWCNT) encapsulated in an epoxy membrane [14] and nanopore created in a polymeric membrane using track-etch method [15]. Adapted from ref. [16]

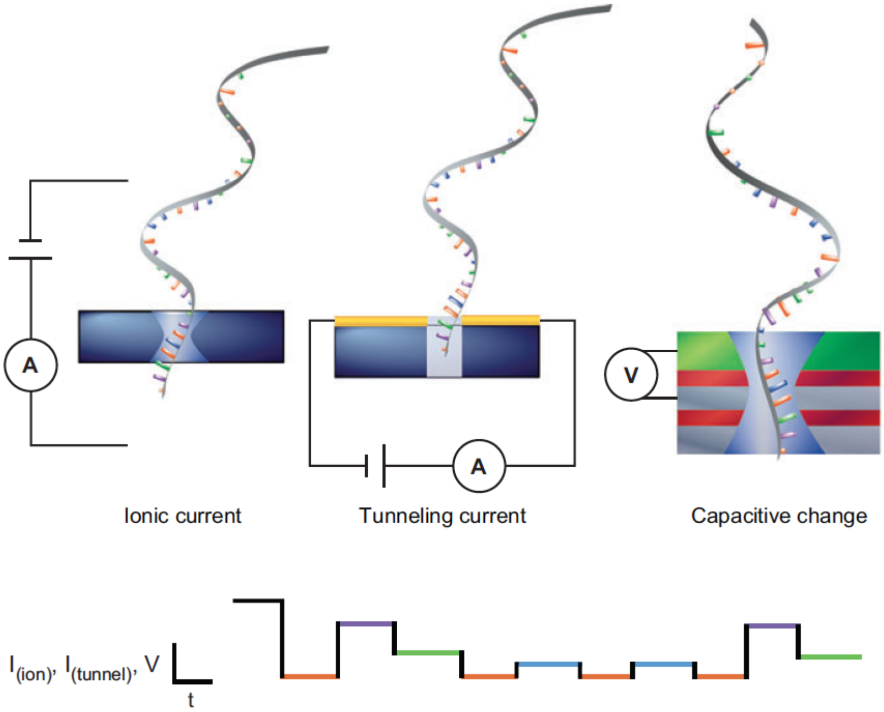

Figure 1.3 Proposed measurement concepts for DNA-sequence readout using nanopore technology. Top from left to right: monitoring the modulation of ionic current [6], tunneling current [17] and capacitive voltage [18]. Bottom: Simplified cartoon illustration of how different types of nucleotides may modulate the measured quantity in a distinctive manner. Adapted from ref. [16]

Naturally occurring nanopores provide reproducible structures with atomic-level precision and have demonstrated great potential in single-molecular studies [4, 19]. However, biological nanopores do suffer from some inherent disadvantages due to certain attributes: a) mechanical fragility and sensitivity of the supporting lipid bilayer; b) susceptibility to experimental conditions such as pH, temperature, solution composition and voltage range; c), difficulty of integration into nanofluidic devices/arrays and solid-state platforms; and d) fixed shape and size [19]. In the case of proteins with a known structure genetic engineering and site-directed mutagenesis allow for some modifications of the pore properties and incorporation of sensing sites [19]. While nanopores contained in thin synthetic membranes can overcome most of these drawbacks, challenges in fabrication and considerable inconsistency in the pore size, conductance level and noise characteristics have so far prevented them from reaching the performance of their biological counterparts [20, 21]. Carbon nanotubes are another important class of solid-state nanopores, which readily provide well-defined nanopores/nanochannels with atomic precision and uniformity. We discuss nanofluidic devices based on carbon nanotubes in section 1.3.

Nanofluidics falls into length scales in which inter-molecular forces often negligible at larger scales such as steric interactions/hydration (~ 1-2 nm), van der Waals interactions (~ 1-50 nm) and electrostatic interactions (Debye screening length ~ 1-100 nm) become significantly important [1]. This transition leads to new properties and phenomena in fluid transport, which can be manipulated and utilized for additional applications such as drug delivery [22], analyte separation [23], water desalination [24] as well as energy conversion and storage [25].

A firm knowledge of ionic conditions and transport in nanofluidics is essential in order to successfully design, characterize and control nanofluidic devices. The basic physical principles of fluid transport in nanoscale are embedded in well-established concepts of science and technology; however, the current knowledge of nanofluidics is still in its infancy [26].

In nanofluidics, both experimental and theoretical studies are similarly significant. Experimental studies require nanopores with known sizes and surface characteristics, while simulation studies require more advanced computing power. While continuum dynamics is quite common in calculating ion transport in micrometer (larger than 1 μm) and sub-micrometer (larger than 100 nm but smaller than 1 μm*)* length scales, it fails to describe the electrolyte behavior in nanochannels narrower than ~ 5 nm. In length scales below ~ 5 nm stochastic dynamics and/or molecular dynamics (MD) simulations are often used to model the systems [1].

1.2 Electrostatics and electrokinetic effects in nanochannels

Nanofluidic systems have very high surface-to-volume ratios resulting from downsizing the channel dimensions. As a result, fluid transport is highly governed by fluid-channel interactions, especially those which are electrostatic in nature [26]. Here, we briefly introduce some of the fundamental concepts of fluid transport in nanochannels.

1.2.1 Electrical double layer

When a solid surface become in contact with a liquid it often acquires a surface charge. The surface charge establishment is usually result from the ionization of surface functionalities or preferential attachment of solution ions on the surface. The electrostatic interactions between the charged surfaces and solution ions strongly influence the fluid behavior in nanofluidic systems [26].

A charged surface in contact with an ionic solution redistributes the ions in its vicinity by attracting the counter-ions and repelling the co-ions. This results in the formation of a counter-ion rich region in proximity to the charged surface (Fig. 1.4). This screening region, called electrical double layer (EDL), maintains the neutrality of the solid-liquid interface and is consisted of two layers: Stern layer and diffuse layer. While in the Stern layer the counter-ions are bound to the surface (immobilized), they are free to move in the diffusion layer. The zeta potential, ζ, is defined as the electric potential at the interface between the Stern and diffusion layers known as shear, or slip, plane [1].

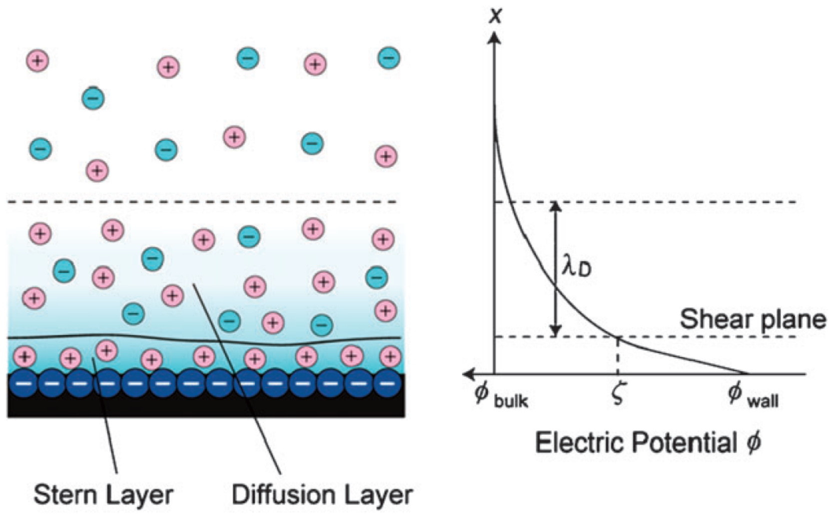

Figure 1.4 Ionic distribution in close proximity of a charged surface. Cartoon illustration of electrical double layer (right). Decay profile of surface potential in the solution perpendicular to the charged surface (left). Adapted from ref. [1].

The electric potential originating from the charged surface decays exponentially in the solution over a characteristic distance given by the Debye screening length, λD:

$$\lambda_D = \sqrt{\frac{\varepsilon_0 \varepsilon_r k_B T}{2N_A e^2 I}} \qquad (1.1)$$

where ε_0 and ε_r are the permittivity of free space and dielectric constant, respectively; $k_B$is the Boltzmann constant, T is the absolute temprature, N_A is the Avogadro number, e is the elementary charge and I is the ionic strength of the electrolyte [1, 26].

The thickness of EDL is related to the Debye length and decreases as the ionic strength of the solution increases. Table 1.1 presents the calculated Debye length values at typical concentrations of a monovalent electrolyte at 25 °C [26].

Table 1.1 Typical Debye lengths (λ_D) for monovalent electrolytes in aqueous solution at 25 °C.

Concentration (M)	Debye length (nm)
10^{0}	0.3
10^{-1}	1.0
10^{-2}	3.1
10^{-3}	9.6
10^{-4}	30.5
10^{-5}	96.3

Figure 1.5 compares the ionic condition in a microchannel with a nanochannel, both with negatively charged walls. The height of the microchannel is much larger than the typical λ_D values (1-100 nm), leaving the fluid inside the channel largely neutral and bulk-like. In contrast, the channel height in the nanochannel is comparable to EDL thickness, resulting in a unipolar solution of counter-ions inside the channel. In this case the ion concentration and electric potential inside the channel can largely differ from the bulk phase [1]. This phenomenon is particularly important in nanofluidic physics and related applications.

Same argument holds for the effect of electrolyte concentration in nanochannels. At low concentrations, EDL thickness becomes comparable to channel height, which makes the channel selective towards counter-ions [26].

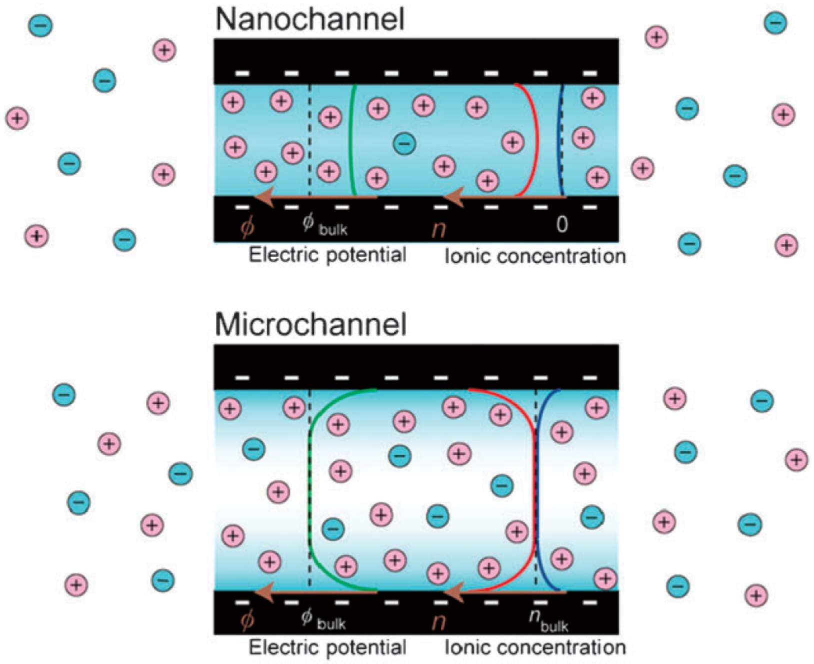

Figure 1.5 Comparison of channel surface charge effect in a nanochannel (upper) and a microchannel (lower). In a nanochannel, the channel height is comparable to Debye lengths, which causes the EDLs overlap to occur. This leads to counter-ion rich solution inside the channel. In a microchannel, Debye lengths are much smaller than the channel height. The solution inside a microchannel mostly has the bulk properties. Green, red and blue lines represent the profile of electric potential, counter-ion and co-ion concentrations inside the channel, respectively. The electric potential (ϕ_{bulk}) and ion concentration (n_{bulk}) in bulk are shown by dash lined.

1.2.2 Electroosmosis

Electrokinetics examines the movement of charged species in fluidic environments, such as water, in the presence of an applied electric field [26]. Here we introduce electroosmosis, which is the most relevant electrokinetic concept for our discussion.

Electroosmotic flow occurs when excess counter-ions in the EDL draw along the solvent molecules adjacent to the channel wall (by viscous coupling) as they move in an electric field parallel to the interface [27]. The liquid electroosmotic velocity is assumed to be zero at the slip plane, increase to a maximum value, v_{eo}, as it is moving away from the wall and finally plateau at a certain distance from the wall [26]. The electroosmotic plug flow is formulated as below:

$$v_{eo} = \mu_{eo} \times E_x \tag{1.2}$$

$$\mu_{eo} = \frac{\varepsilon_o \varepsilon_r \zeta}{\eta} \tag{1.3}$$

where μ_{eo} is electroosmotic mobility, E_x is the electric potential parallel to the surface and η is the dynamic viscosity of the liquid [26].

Due to the overlapping EDLs in nanochannels, the electroosmotic flow deviates from its plug form and becomes a function of electric potential distribution, $\Psi\,(z)$, inside the channel [26]:

$$\nu_{eo} = \mu_{eo} E_x \left(1 - \frac{\psi\,(z)}{\zeta}\right) \quad (1.4)$$

1.3 Carbon nanotube based-nanofluidic systems

Carbon nanotubes are an important class of solid-state nanopores/nanochannels. They offer an excellent template for fundamental study of nanofluidic systems by readily providing a simple, well-defined and atomically smooth nanostructure with superior chemical and mechanical stability [28, 29]. Additionally, the structural simplicity makes them appealing in simulation studies.

Carbon nanotubes hold a great potential for technological applications as well due to several factors: a) CNTs can be synthesized in various diameter sizes (from a few angstroms up to tens of nanometers) without the cost and complication of fabrication procedures necessary for other type of solid-state nanopores [30]; b) CNTs have atomically-smooth and uniform structures over large lengths (few millimeters), which make them compatible with current fabrication technologies [1, 31]; c) CNTs have adjustable dimensions and surface chemistry, which make them compatible with both solid-state and biological platforms [32]; d) in addition to individual CNT devices, millions of CNTs can be easily incorporated into a membrane to form an array device [24, 33, 34]; e) transport in CNTs is almost frictionless leading to ultra-fast flow rates and throughputs [35, 36], f) functionalization of CNTs at their openings provides a valuable knob to control the ions/molecules flow in sensing, gating and filtering applications [37-39].

Over the past few years, CNT-based nanofluidic devices have been the subject of many computational studies extending from mass transport fundamentals to CNT toxicity, biocompatibility and interactions with biomembranes for biomimetic purposes [28, 34, 38, 40-45]. Initially, Hummer and coworkers studied the interaction of water molecules with a 1.34 nm long (6,6) CNT with MD simulations [35]. They were the first to demonstrate that water molecules readily enter the hydrophobic interior of the nanotube. They explained this counter-intuitive observation through a reduction in free energy, as molecules form an ordered structure in the confined interior of the nanotube. The presence of water molecules inside CNTs has been confirmed by various experimental techniques such as transmission electron microscopy (TEM) [46], IR microscopy [47] and X-ray diffraction [48]. Water molecules are believed to pass through the smooth interior of CNTs nearly frictionless, resulting in flow rates orders of magnitude faster than that predicted by classical hydrodynamics [35]. Subsequent simulation studies have demonstrated that beside water molecules, ions and other small molecules, such as long polymers [49], DNA strands [50] and RNAs [51], would also enter small diameter CNTs.

On the experimental side of research, primary experiments involving fluid transport through both individual and collections of CNTs (CNT membranes) have been reported [28, 34, 38, 40-42]. Although the number of computational studies over the past few years has rapidly grown, experimental data confirming the simulation results has remained sparse, especially at the single nanotube level.

Carbon nanotube membranes are often fabricated by casting a thin layer of polystyrene polymer or evaporating a thin layer of silicon nitride on a dense, vertically grown CNT array [39, 40]. The nanotube ends then become open by treating the membrane in oxygen plasma. The flow of gases, water and ions measured through CNT membranes show significantly enhanced mobility values compared to other types of membranes [36, 40]. CNT membranes have displayed great potential for chemical separation and water desalination applications given their performance and relative ease of fabrication.

While membrane studies yield statistical results, devices based on a single nanopore allow for precise examination of transport mechanisms and careful manipulation of translocating species [52-54]. In 2003, Ito and coworkers fabricated one of the first Coulter counter fluidic devices based on a single multi-walled carbon nanotube (~ 130 nm in diameter incorporated in an epoxy membrane) to determine the size and surface charge of polystyrene nanoparticles [14]. In 2007, Shashank and coworkers reported a study on fluid flow through single carbon nanopipes (~ 200-300 nm in diameter) [55].

It was only in the past few years that fabrication and electrical measurement of ionic flow through individual sub-2nm CNTs (where confinement effects play a major role) has been experimentally reported [41, 42, 56]. Our group, in collaboration with S. Lindsay group, was able to electrically measure the transport of electrolyte and small DNA molecules through individual CNTs (1-2 nm in outer diameter and 2 μm in length) in a solid-state device [41]. Recently, Liu et al. were able to electrically measure electrolyte and DNA transport in ultra-short single-walled carbon nanotubes (SWCNTs), 1-2 nm in diameter and 5-10 nm in length, incorporated into a lipid bilayer using a microinjection probe [42]. Strano group fabricated nanofluidic devices based on a horizontal array of CNTs (1.3 to 2.3 nm in diameter and 500 μm in length) and observed oscillations in ionic current (stochastic pore blocking events) as individual translocating cations obstruct the proton current [56]. In subsequent studies, they removed the unwanted nanotubes from the silicon surface using a razor blade and performed experiments on individual nanotubes [57, 58].

Despite significant progress in the past few years, the underlying physics of electrolyte permeation through narrow CNTs and contributing factors are still far from understood and demand further experimentation, especially at the single nanotube level.

1.4 Biological nanopores and nanochannels

1.4.1 Introduction

Many vital biological processes take place in nano-sized pores. For instance, the nuclear pore complex (NPC) is responsible for the protected exchange of mRNA and proteins between the nucleus and cytoplasm; some viruses release their genome into the host cytoplasm through the pores they create in the host membrane. Transmembrane protein ion channels regulate the transport of ions and small molecules across the cell membrane by responding to the environmental stimuli [20].

Transmembrane ion channels are incorporated into the cell membrane and regulate ion fluxes across the hydrophobic lipid bilayer through unique gating and/or selectivity mechanisms [59]. Biological ion channels are found across all living organisms and control a large number of cellular functions including osmotic regulation, electrical activities and nervous signal transmission, muscle contraction and responses to drugs and hormones [60]. Consequently, ion channel malfunctions result in some of the most challenging disorders (e.g. diabetes, cystic fibrosis, epilepsy, cardiac dysrhythmia and ataxia) [60-63], which makes them highly studied in new drug and diagnostic research [64, 65].

Transmembrane protein ion channels are the nature's ultimate nanochannels, in the sense that they simultaneously exhibit both high ion selectivity and conduction rate [59]. For instance, potassium channels can be up to 1,000 times more permeable to K^+ than the smaller ion Na^+ [10]. The remarkable ion selectivity in ion channels is supplemented by high ionic throughputs reaching the diffusional limits [26, 59].

Ion permeation in biological ion channels is often regarded as a multi-step process. First, the ions diffuse in the solution to find the channel entrance. Second, ions often need to loose some of the water molecules in their hydration shells in order to be accommodated by the pores. The interaction of ions with pore binding sites can partially compensate for the loss of the tightly bound water molecules. Ions then translocate along the pore and regain their hydration shells upon exit [59]. Every step of ion permeation in ion channels is often associated with a change in the free energy [59]. Ions may encounter several free energy barriers while translocating through the pore [59]. Unraveling the free energy barrier landscape of ion permeation is a key factor in understanding the underlying mechanism of ion transport, selectivity and gating in ion channels.

Despite extensive research over the past few decades, understanding the basic principles underlying the energetics and dynamics of transport mechanisms through these biochannels is still far from complete. This limited understanding is due to the irregular, complex and flexible structure of ion channels, with both hydrophobic and a hydrophilic regions and highly inhomogeneous charge distribution [66]. Furthermore, several factors are involved in shaping ion channel function, which makes determining their individual contribution difficult [59, 66]. Lastly, determining the crystallographic structure of transmembrane proteins has remained a challenge over the years, as this class of proteins has limited solubility in water and denatures in organic solvents. It was only in 1998 that three-dimensional atomic structure of potassium channels (KcsA) was determined by X-ray crystallographic techniques (Fig. 1.6) [10].

1.4.2 Biomimetic designs and applications

Despite all of the recent advancement, none of the man-made nanopores/nanochannels to date have been able to achieve the remarkable performance of their biological counterparts [26]. Many researchers have been inspired by nature’s superiority, leading them to continue to try and reproduce the functionality of biological nanopores in synthetic devices [67]. Advances in biomimetic research may be significant for the future of nanomedicine [68]. For instance, properly engineered artificial ion channels can selectively insert into membranes of specific cell types (e.g. bacteria or cancer cells) and kill them by targeting certain drugs or destroying their cell potential [69]. Artificial nanochannels have been designed to mimic the ion-responsive ion channels [70-72], receptor-mediated transport through NPC [73, 74] and ionic current rectification [75] observed in natural nanopores.

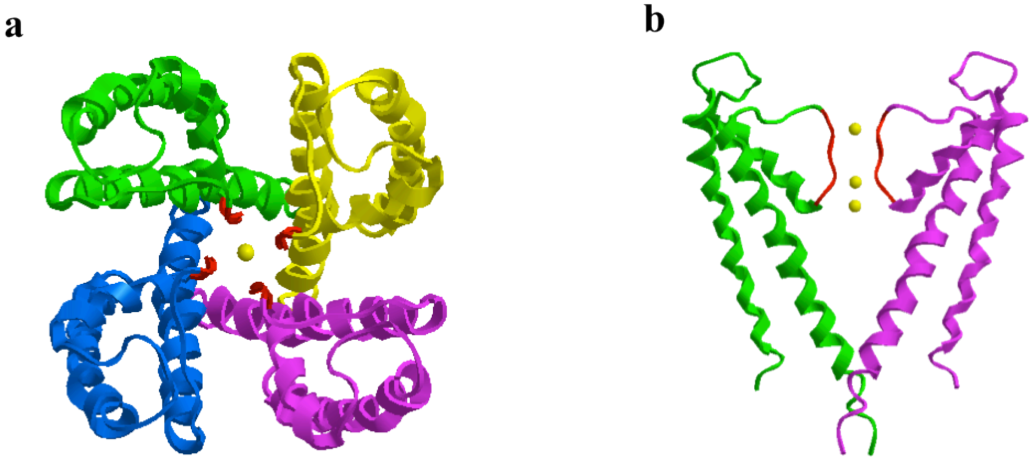

Figure 1.6 Crystallographic structure of the potassium channel (KcsA) (PDB ID: 1BL8) [10]. The subunits, surrounding a central pore, are displayed in different colors. The selectivity filter, colored red, contains residues with carbonyl groups, which are essential for K+ selectivity. Potassium ions are illustrated as yellow spheres. a) Stereoview of the tetramer from the extracellular side. b) Stereoview from a different perspective. Only two of four subunits of the tetramer are shown.

Single-walled carbon nanotubes are proposed as structural analogues of transmembrane protein ion channels and are among highly promising candidates for mimicking the general properties of protein ion channels [68, 76]. Both carbon nanotubes and biological ion channels have an inner diameter, which is nanometer-sized as well as a hydrophobic core. The mechanism of water transport through both SWCNTs and biological pores is also proposed to be distinctively similar through the cooperative, pulse-like movement of hydrogen-bonded water along the channel axis [35]. Water molecules are believed to pass through the smooth interior of CNT nearly frictionless, resulting in flow rates orders of magnitude faster than that predicted by classical hydrodynamics [35, 40]. Ion selectivity beyond the steric sieving is also assumed to be achievable in SWCNTs, either intrinsically [77] or with the assistance of pore charged functionalities [45, 76, 78, 79]. Lastly, the length and surface chemistry of SWCNTs can be adjusted (e.g. by attaching proteins or antigens to the exterior of the tubes or by wrapping polymers around them) in order to improve their solubility and bio-integrability [32, 69, 80].

In the past few years, biomimetic CNT-based templates inspired by design rules and insights from biological systems have been the topic of numerous MD simulation studies [45, 81, 82]. It has been shown that water and ion permeation in protein channels and derivatized SWCNTs share several common features, including ultra-fast flow rate [35], changes in ions' hydration state [83], ions chaperon effects [77, 78] and concerted movements [84]. There were also several attempts to mimic the selectivity filter in ion channels in order to design highly ion selective nanotubes. For instance, in two separate simulation studies, T. A. Hilder and coworkers demonstrated how placing carboxyl (or carbonyl) groups at the rim of the nanotube can achieve high cationic (or anionic) selectivity [45, 78]. More complex carbon nanotube-based designs were also envisioned in order to largely mimic the transport characteristics of specific biological pores such as antibiotic Gramicidin-A [82], potassium channels [85] and chloride selective channels [45].

Advances in the field of biomimetic research can help us to better comprehend the underlying mechanisms of ion permeation and selectivity which transpire in complex biological systems. Additionally, this research may eventually lead to the development of artificial biomimetic nanopores able to reproduce some of the most critical biological ion channel properties [82].

1.5 The present work

In this study, we experimentally investigate ion permeation in individual narrow carbon nanotubes and demonstrate that, in addition to structural similarities, ion conduction in CNTs and many biological ion channels share common characteristics. There is substantial evidence that permeation properties and functionalities of many different protein ion channel types can be strongly influenced by the presence of fixed charges around the pore entrance [86]. For instance, the high conductance Ca^{2+}-activated K^+ channel (CaK) is thought to carry ionized carboxyl groups near its pore mouth, which electrostatically affect ionic conductance, ionic blockade and gating properties of the protein [87]. The role and chemical identity of these charges have been extensively studied, even in the absence of structural information. They are often determined by experimental manipulations of surface electrostatics, such as changing the ionic strength, composition or pH of the bath solutions or chemical modification of the protein using group specific reagents or site-directed mutagenesis [86]. In this work, following the same methodology, we provide several lines of evidence that the deprotonated carboxyl groups present at the CNTs' entrance influence ion permeation through the same electrostatic mechanism as the charged groups in the entrance region of many protein ion channels.

CHAPTER 2

Single-Nanotube Electrophysiological Measurement Platform

2.1 Introduction

The experiments reported here have been carried out in a microfluidic set-up similar to that used by Liu et al. [41]. In brief, the device consists of two fluidic reservoirs, patterned in a polymethyl methacrylate (PMMA) resist, connected solely through the interior of one CNT, ≤ 1.5 nm wide and 20 μm long, lying on a silicon substrate (Fig. 2.1). Oxygen plasma treatment is used to cut the unwanted parts of the CNT and open both of its ends. A polydimethylsiloxane (PDMS) polymer block with microfluidic channels is then placed on top of the PMMA layer to keep the two reservoirs completely separated and sealed apart while delivering liquid to each one individually.

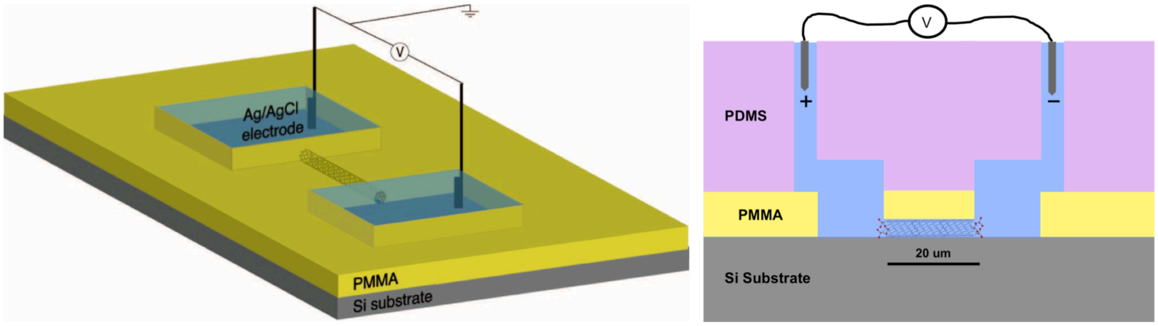

Figure 2.1 Schematic of a carbon nanotube nanofluidic device (left). Two aqueous reservoirs patterned in PMMA resist are connected through the interior of only one carbon nanotube. Cross-sectional view of the device (right). A PDMS microfluidic device delivers the liquid to the reservoirs.

We also examined leakage devices for our second type of nanochannel, as a parallel ion conduction pathway within the same device architecture and measurement set-up. This helps to isolate the effect of CNT(s) on ionic transport from any other possible source.

The two reservoirs in leakage devices were connected through the cracks embedded in the PMMA surface roughness, which arises after an intentionally aggressive oxygen plasma treatment (Fig. 2.2). The PDMS block in the leakage device does not provide the complete seal and allows a small leakage of ionic current between the two solutions.

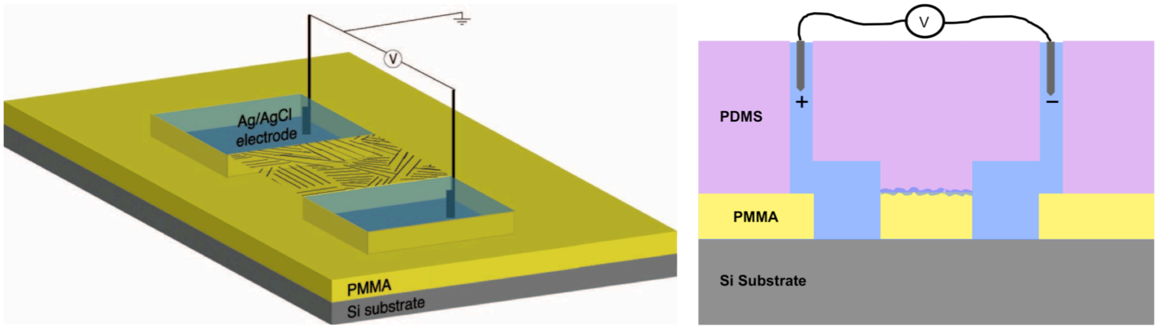

Figure 2.2 Schematic of a leakage device (left). Two aqueous reservoirs patterned in PMMA resist are connected through the cracks embedded in the PMMA surface roughness. Cross-sectional view of the device (right). A PDMS microfluidic device delivers the liquid to the reservoirs.

2.2 Device fabrication

2.2.1 Carbon nanotube growth

2.2.1.1 Chemical vapor deposition method

Carbon nanotubes are often synthesized using physical techniques (e.g. arc discharge [88] and laser ablation [89]) or chemical methods such as chemical vapor deposition (CVD) [90]. Carbon nanotubes created with physical techniques have shorter lengths (≤ 1-2 μm) and higher defect density (after solution processing) compare to CVD grown nanotubes[91, 92]. In order to make devices out of physically-grown nanotubes, a prepared CNT suspension (often with a surfactant for stabilization) is deposited on the substrate [93, 94]. Achieving well-separated nanotubes with this technique is challenging, however, as nanotubes tend to bundle up [95, 96]. Alternatively, CVD methods allow us to directly grow well-separated individual CNTs on the substrate [97]. CVD-grown CNTs are quite long (up to a few millimeters) and are high quality (low defect density) [98]. The CVD process also allows for better control over CNT properties such as tube diameter distribution, orientation and length [58, 98].

In a typical CVD process, carbon precursors are decomposed at high temperatures to form nanotubes. The process is catalyzed by metallic nanoparticles, which also serve as nucleation sites for the nanotube growth [30, 98]. At the growth temperature, the atomic carbon has limited solubility in the metallic nanoparticles. Once the particles are saturated, the excess carbon precipitates out in the form of tubular carbon with sp^2 hybridization. The parameters in the growth process are chosen in a way that the tubular structure of carbon, which lacks any dangling bond, would be the thermodynamically-favored allotrope [98]. Parallel arrays, or networks, of nanotubes can be obtained on a flat surface or over trenches using this technique [99].

2.2.1.2 Experimental procedure

In this study, we synthesized our nanotubes using the CVD technique in a set-up shown in Fig. 2.3. Iron-stored ferritin proteins were used as the catalyst [100] and ethanol was used for the carbon source [101]. The CVD system is then connected to the H_2 (reducing gas) and Ar (carrier gas) tanks and the gas flow rates are measured and controlled by mass-flow controllers. There are two flow channels available between the mass-flow controllers and the CVD furnace; the first channel (ch.1) is used when only H_2 and/or Ar gas are flowing through the system, while the second channel (ch. 2) allows the gasses to bubble through ethanol in order to carry ethanol vapors into the CVD chamber.

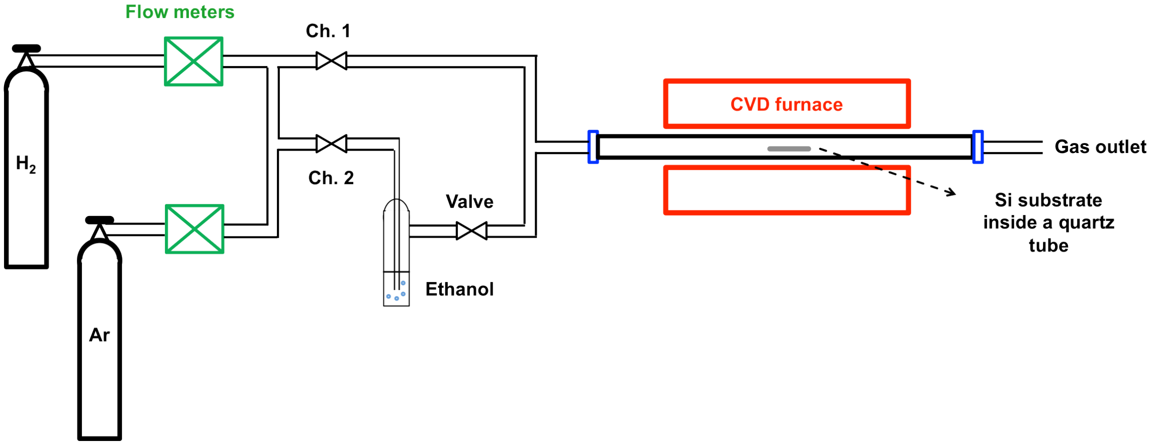

Figure 2.3 Schematic of the CVD set-up used for synthesizing carbon nanotubes.

We prepared the catalyst by diluting the commercially-available ferritin proteins (Sigma-Aldrich Corp., St Louis, MO) in deionized (DI) water (200 times v:v). We then brushed the diluted solution onto the edge of a silicon wafer. The silicon substrates were 1.0 cm^2 in size and had a 300 nm-thick thermally grown SiO_2 layer on their surface. Just before usage, the silicon substrates were cleaned in piranha solution (a 7:3 mixture of concentrated sulfuric acid with 30% hydrogen peroxide) at 70 °C for 30 minutes then rinsed with DI water and dried using a N_2 gun. The substrates were placed on a quartz sample boat with the catalyst lines facing the gas flow entrance in the center of a 1 inch wide-quartz tube in the CVD furnace.

In order to remove all the organics and form iron oxide nanoparticles, samples were annealed in air at 800 °C for 10 minutes. The CVD system was then isolated from ambient air and flushed with Ar gas to remove all the remaining oxygen. In order to reduce and activate the catalyst nanoparticles, a mixture of Ar and H_2 with flow rates of 642 and 115 standard cubic centimeters per minute (sccm), respectively, flowed through the system at 800 °C for a period of 20 minutes. The furnace temperature was then ramped up to 890 °C over 10 minutes and the Ar and H_2 flow rates were reduced to 138 sccm and 18 sccm, respectively. Once the furnace temperature reaches 890 °C, carbon nanotube growth is initiated by switching the valves to second channel and introducing ethanol vapor to the CVD chamber. The gas mixture, bubbling through ice-cold ethanol, carries ethanol vapor as the carbon source to the CVD chamber. After 1 hour, the CNT growth process was stopped by switching to the first channel and the system was allowed to cool down (to room temperature) under the same argon and hydrogen flow rates.

2.2.1.3 Results

Oriented carbon nanotubes up to 1 cm long were grown on silicon substrates from the ferritin catalysts using the CVD method. The nanotubes were grown parallel to the gas flow direction and almost parallel to each other as shown in the scanning electron microscope (SEM) images in Fig. 2.4. SEM images were taken on a Hitachi microscope (S-4700 FE-SEM) at 0.8-1.0 kV. SEM imaging allows for examining the density and length of the CVD-grown carbon nanotubes. We measured the outer diameter distribution of as-grown CNTs using tapping-mode atomic force microscopy (AFM) as shown in Fig. 2.5. The AFM images were taken on a Veeco Dimension Icon AFM. The outer diameter of nanotubes was centered on 1.5 nm.

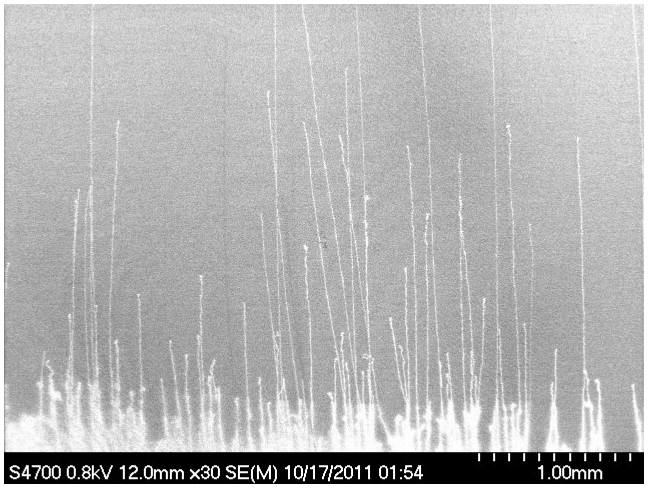

Figure 2.4 SEM image of flow-grown carbon nanotubes from ferritin catalyst using CVD method.

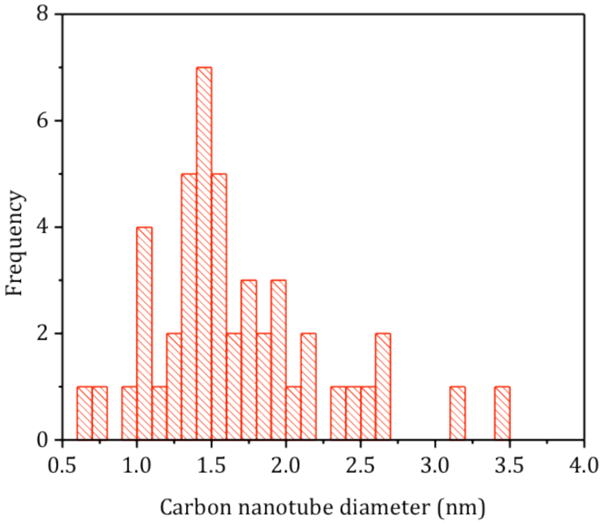

Figure 2.5 The outer diameter distribution of carbon nanotubes grown from ferritin catalyst.

CVD methods allow for growing CNTs on flat surfaces as well as over narrow slits. Figure 2.6 shows the SEM images of nanotubes grown over a 1.5 mm × 100 μm window in silicon nitride. Suspended CNTs allow for further characterization using transmission electron microscopy and Rayleigh scattering spectroscopy to determine the number of tube walls, chirality, etc [102]. They also provide a platform for suspended nanotube experimentation.

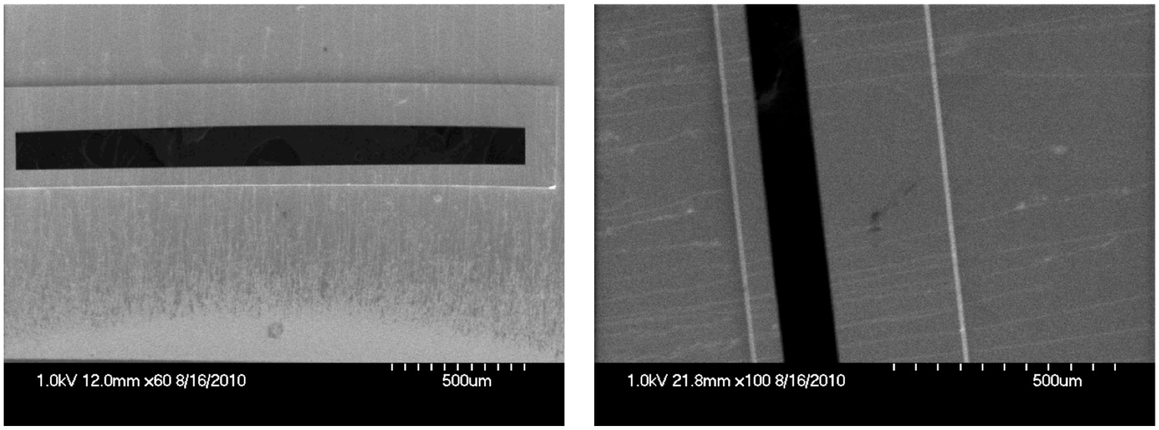

Figure 2.6 SEM images of CVD-grown nanotubes over an open window in a silicon nitride membrane

Silicon, silicon nitride and quartz are the most common substrates for CNT growth as they can tolerate the high temperatures required for CVD processes (~ 900 °C). The CVD-grown CNTs, however, can be easily transferred to a new substrate such as glass, as illustrated in Fig. 2.7 [103]. We utilized this method with some modifications to transfer our CVD-grown nanotubes onto a new substrate.

First, a thick layer of PMMA (~ 600 nm) is spun coated on a silicon substrate (with CNTs) and annealed at 170 °C for 5 minutes. The resist-coated substrate is then immersed in a 1.0 M solution of aqueous KOH at 80 °C until the PMMA layer comes off (~ 1 hour). The basic solution etches away the thin SiO_2 layer on the silicon substrate and releases the PMMA layer. The PMMA film floating on the solution contains the CNTs. After KOH solution is replaced by DI water through several washing cycles, the PMMA film can be gently scooped out by a new substrate. The sample is then air dried and annealed at 50 °C for 5 minutes to increase the adhesion of PMMA film to the surface.

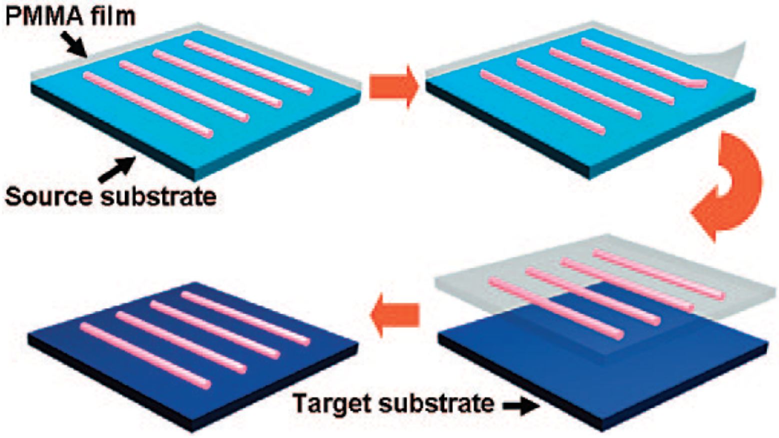

Figure 2.7 Illustration of a common CNT transfer method mediated by a thin layer of PMMA. Adapted in part from ref. [103]

The PMMA polymer can be removed from the substrate by immersing the sample in acetone. Figure 2.8 presents the SEM images of carbon nanotubes before and after transferring the CNTs onto a glass coverslip substrate. The transferred CNTs can be used in various optical microscopy experiments. For instance, total internal reflection fluorescence (TIRF) microscopy can be utilized in the studies combining CNT nanofluidic devices with fluorescently tagged molecules.

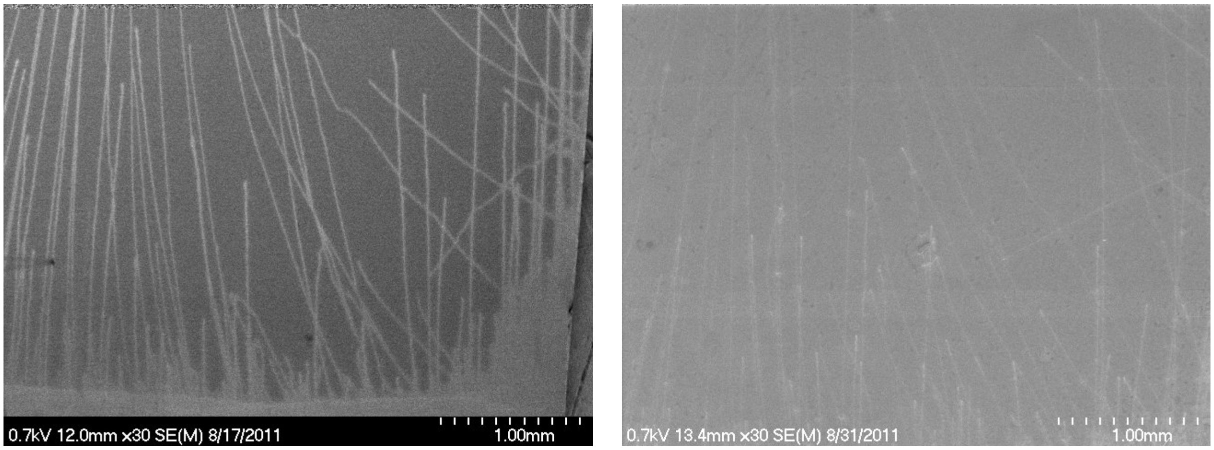

Figure 2.8 SEM images of carbon nanotubes before (left) and after (right) being transferred to a glass coverslip substrate. The SEM image quality of the glass substrate is low due to the buildup of charge on the insulating substrates.

2.2.2 Patterning the substrate with gold markers

After we examined the nanotube growth quality (e.g. tube density and length) by SEM, we patterned the substrate with a series of gold markers. The markers provide a coordinate system on the surface and also help with the alignment step, in which two reservoirs are patterned on top of the selected nanotubes. Figure 2.9 shows the latest version of the index marker used in this study designed in DesignCAD LT 2000 software. The 8 mm^2 pattern consists of an array of four markers (marker block); rows marked by letters and columns marked by numbers.

We have fabricated our devices with electron beam lithography (EBL) because EBL offers high resolution (~ tens of nanometers), uses a clean and nanotube friendly resist PMMA and allows for easy customization since it does not require a mask. In order to pattern the substrate for gold deposition, a 600 nm-thick layer of PMMA (PMMA 950K A6, MicroChem Corp., Newton, MA) was spun coated on the substrate, and baked at 180 °C for 5 minutes. The designed marker pattern was then written on the PMMA resist using an electron-beam writer (NanoBeam LTD, Cambridge, UK). With sufficient dosage, the electron beam will break down the polymer chains, which increases the solubility of exposed resist areas in the developer. We developed the resist by immersing the samples in a 1:3 mixture of isopropyl alcohol (IPA) and methyl isobutyl ketone (MIBK) (NANO™PMMA and copolymer developer, MicroChem Corp., Newton, MA) for 2 minutes, then rinsing in IPA and blow-drying with N_2 gun.

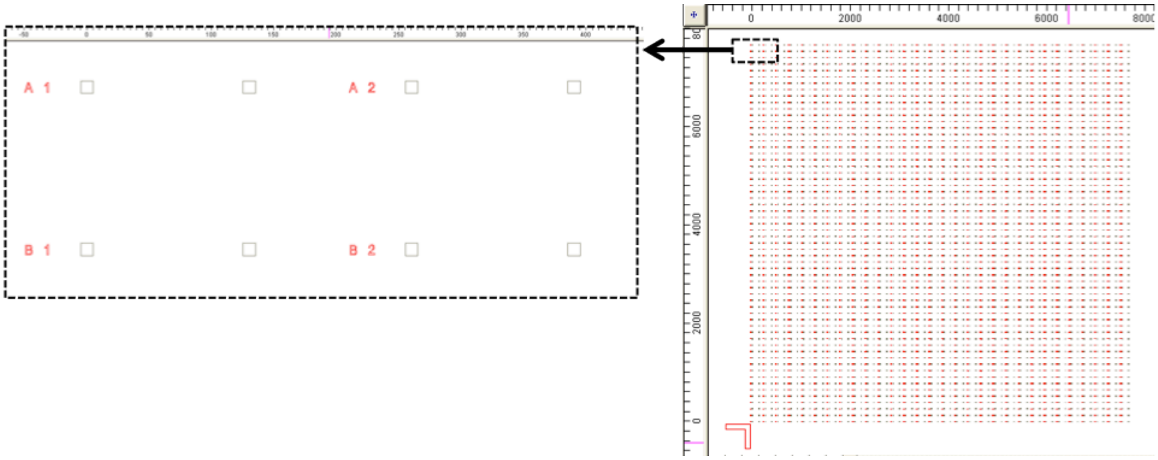

Figure 2.9 The marker pattern designed in DesignCAD LT 2000 software. The pattern consists of an array of four markers (marker block); rows marked by letters and columns marked by numbers.

Subsequently, 3.0 nm of Cr (used as an adhesive layer) and 30.0 nm of Au were uniformly deposited on the patterned resist using an electron beam evaporator (Angstrom EvoVac deposition system or Semicore SC2000 electron beam evaporation system). We then place the samples in acetone overnight; this removes all the PMMA from the surface and leaves behind the gold markers.

2.2.3 Nanotube selection and characterization

The presence of gold index markers on the surface allows us to locate and characterize the nanotubes individually. We used SEM (Hitachi microscope S-4700 FE-SEM at 1 kV) to locate the nanotubes with respect to the gold markers (Fig. 2.10.a) and tapping-mode AFM (Veeco Dimension Icon AFM) to determine their outer diameter (Fig. 2.10.d). We only selected nanotubes with diameters ≤ 1.5 nm for nanofluidic device fabrication. In addition, suitable nanotubes for device fabrication should preferably be straight and well separated (Fig. 2.10.b and 2.10.c).

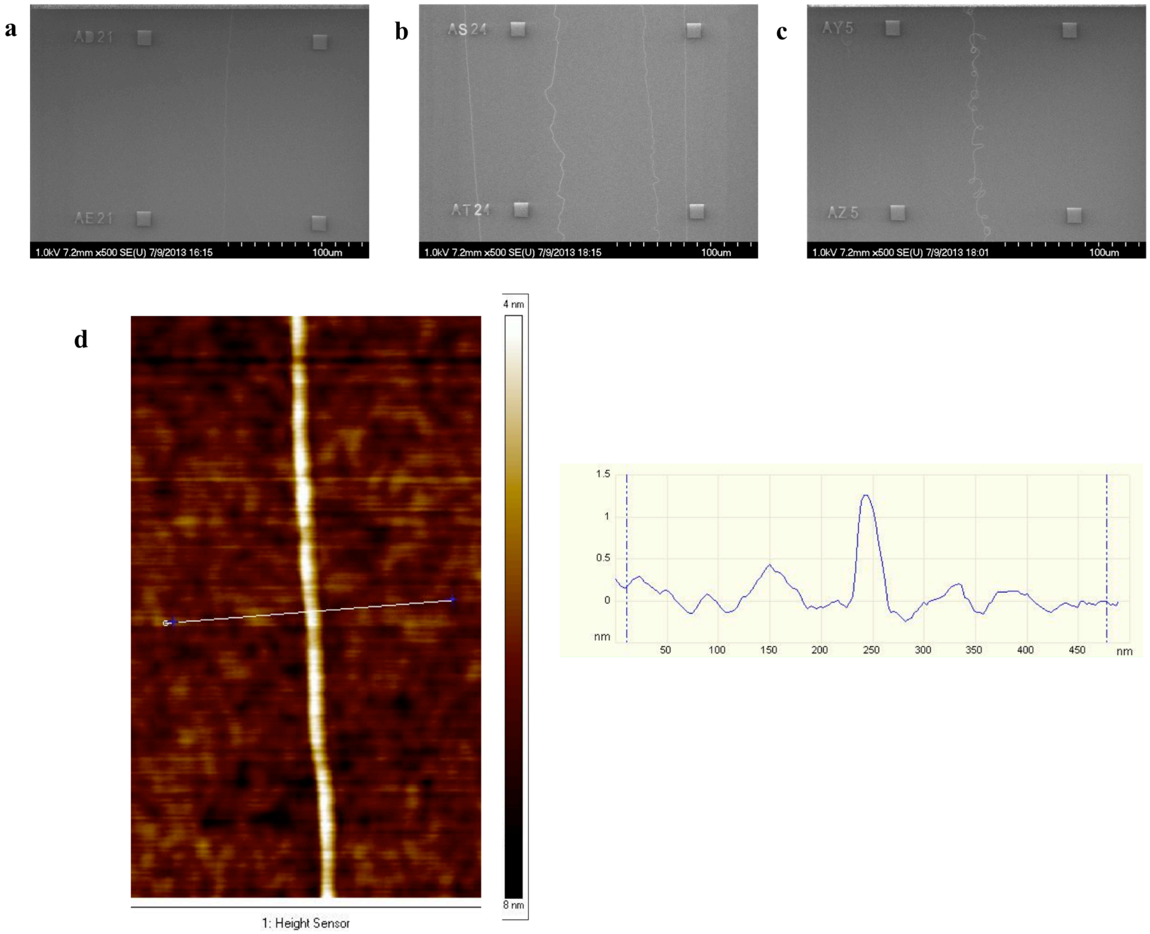

Figure 2.10 CNT characterization. SEM images of CNTs with respect to gold markers. a) desirable CNT for device fabrication. b, c) undesirable CNTs. d) Height sensor-AFM image of a carbon nanotube ~ 1.3 nm in outer diameter.

2.2.4 Fabrication of two fluidic reservoirs

Once we selected certain nanotubes for device fabrication, we imported the corresponding SEM images into a design software and scaled their size to match the design dimensions, as demonstrated in Fig. 2.11. This allows us to ascertain the location of chosen nanotubes and the reservoirs to be patterned on the coordinate system.

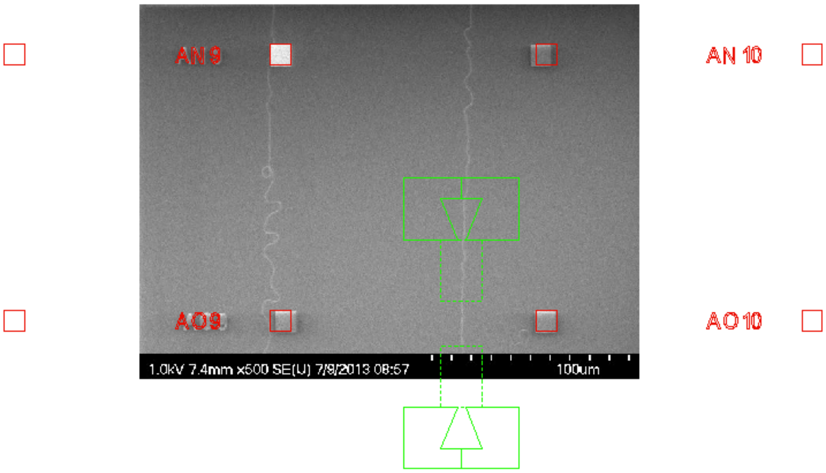

Figure 2.11 Positioning of devices. The imported SEM image of a selected nanotube in the design software allows for determination of reservoir coordinates.

When the tentative location of reservoirs is determined, the substrate is coated with a 600 nm-thick PMMA resist and baked at 180 °C for 5 minutes. The reservoir patterns are then written on the PMMA layer using EBL. After the resist is developed (see section 2.1.2), there are two open cavities in PMMA (reservoirs) precisely on top of the selected nanotubes. An optical microscope image of two reservoirs patterned in the PMMA resist along with its corresponding SEM image are shown in Fig. 2.12.

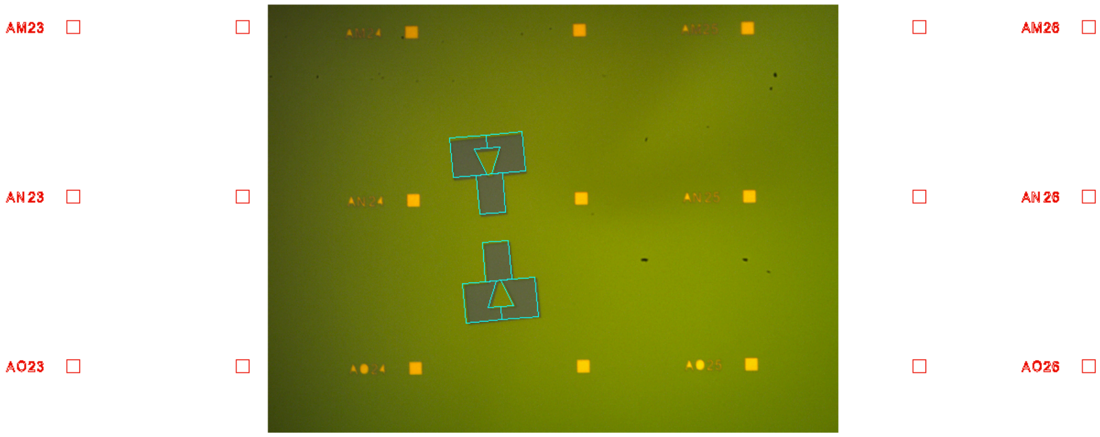

Figure 2.12 Optical microscope image of patterned reservoirs in PMMA resist imported to the design file.

Once two reservoirs are patterned in PMMA along the length of one CNT, the exposed areas of the nanotube need to be removed in order to open the two ends of the CNT and have a fluidic bridge between the two reservoirs. This is achieved by treating the sample to oxygen plasma etch (Technics Series 800 reactive-ion etching (RIE) machine, 50 W RF power, 250 mTorr oxygen) for 10 seconds. The parameters used in the oxygen plasma treatment step are particularly important because weak plasma does not remove the unwanted parts of the nanotube while strong plasma damages the PMMA barrier, causing a leakage between the two aqueous compartments. The leakage devices were exposed to oxygen plasma (with similar parameters) for 30 seconds instead.

2.2.5 Fabrication of the microfluidic device

2.2.5.1 Introduction

In fabricating microfluidic devices, polymers offer several advantages (e.g. when compared to silicon and glass) due to their tunable physical properties and relatively simple and inexpensive fabrication procedure [104-106]. In particular, the soft elastomer PDMS has become ubiquitous in microfabrication, specifically in microfluidics, due to its desirable properties; PDMS unique properties include its thermal resistivity, gas penetrability, easy compatibility with proteins and transparency (allowing for optical microscopy down to 280 nm) [107]. [108-113]. In addition, PDMS provides elastomeric properties that allow the material to conform to most materials, making it readily integratable with many devices [106].

In this study, we have utilized a two-layered PDMS microfluidic structure to deliver aqueous solution to the patterned reservoirs while keeping the two fluidic compartments completely sealed apart. We have taken the common soft-lithography approach (microscale molding process) for fabricating structures in the PDMS films [114]. In this technique, pattern is transferred from a mold master to a soft elastomer. A typical mold fabrication process and replica molding of PDMS is outlined in Fig. 2.13. In the next sections, we discuss the design and fabrication details of our two-layered PDMS fluid delivery structure.

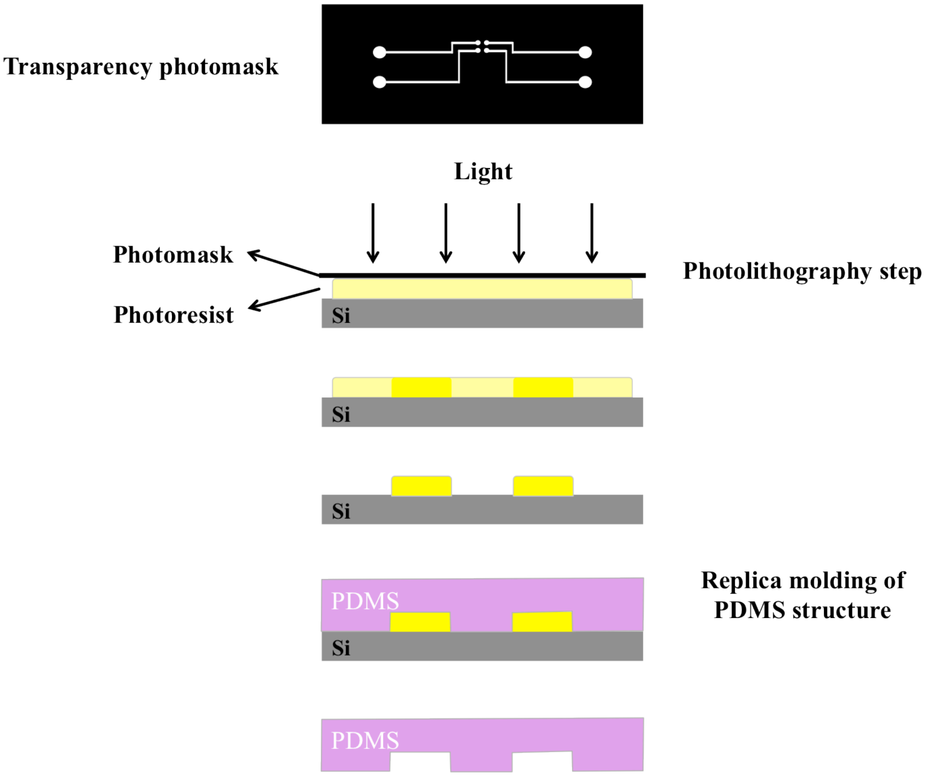

Figure 2.13 Schematic of mold fabrication process and replica molding of PDMS microfluidic structures [106].

2.2.5.2 Microfluidic design

Deformations of PDMS films and/or imperfections in the seal formed at the PMMA and PDMS interface can lead to ionic current leakage. In order to minimize the chance of leakage between the two reservoirs, we designed a two-layered PDMS microfluidic structure. Figure 2.14 shows the design of channels embedded in the top and bottom PDMS layers. In a complete device, the channels are embedded in the bottom faces of the PDMS layers. In this design, liquid travels a very short distance at the interface of PMMA and PDMS and the majority of fluidic channels are embedded between the two

PDMS layers. This design significantly reduces the possibility of ionic current leakage between the two reservoirs.

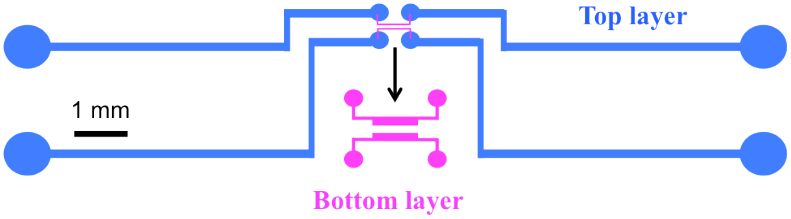

Figure 2.14 PDMS microfluidic design.

2.2.5.3 Fabrication of the silicon mold

As mentioned before, we prepared our PDMS microfluidic structures using a soft-lithography method [115], see Fig. 2.13. A silicon mold, patterned using either optical lithography or deep RIE, is commonly used for laboratory applications. For our master mold, we used optical lithography to pattern a layer of SU-8 negative epoxy photoresist on a silicon substrate. SU-8 is one of the most widely used casting media for microfluidic structure fabrication with a PDMS base. The process starts by spin coating a 20 μm-thick layer of SU-8 (SU-8 2025, MicroChem Corp., Newton, MA) onto a silicon substrate. The thickness of the SU-8 layer determines the channel height in the PDMS microfluidic structure. The silicon substrate was cleaned using piranha solution and baked using a contact hot plate at 200 °C for 5 minutes (for dehydration) shortly before use.

Optical lithography requires a photomask in order to transfer a pattern to the photoresist. Depending on the required resolution, two types of masks are typically used, a), a quartz photomask with a patterned chromium layer deposited on its surface; and b), a high-resolution print on a thin polymer transparency film. We used the latter as the photomask in our fabrication process. After mounting the photomask on top of the SU-8 layer, the sample was exposed to UV radiation (on a MA-6 mask aligner, SÜSS MicroTec AG, Garching, Germany), post-baked on a hot plate and developed. The parameters used in exposure, post-exposure bake and immersion development steps were according to the manufacturer's instructions. SU-8 is a negative photoresist; the exposed area of the resist becomes cross-linked after the exposure and serves as casting features on the finished mold master.

The mold fabrication process is completed when the silicon master is salinized. This was performed by placing a drop of silanizing agent in a desiccator containing the master under the vacuum for approximately 3 hours. During this time the compound evaporates and forms a monolayer of silane on the master surface. This step prevents the PDMS from adhering to the master during the casting process and thus making the peeling of the produced PDMS structure smoother.

2.2.5.4 Replica molding of PDMS microfluidic structures

PDMS is an elastomer with excellent mold-release properties and can replicate features down to nanoscale. Once the mold master is constructed, the Sylgard 184 silicone elastomer base and its curing agent (cross-linker) from Dow Corning are thoroughly mixed in a 10:1 weight ratio. A vigorous stirring is necessary for a thorough mixing. The absolute amount of reagent depends on the size of the petri dish and the desired thickness of the final PDMS layers. When we increase the ratio of the cross-linker in the mix, we end up with a more rigid PDMS structure [116]. Upon mixing the reagents, bubbles (entrapped gasses) are produced in the mixture, which must be fully removed. The bubbles are removed by placing the mixture under vacuum for ~ 2 hours.

The viscous, bubble-free liquid is then poured over the master (in a petri dish) and placed in an oven at 65 °C for 24 hours. Once cured, the PDMS is peeled off of the master, cut as desired, and pasted onto a flat surface of a cleaned glass side (channel-side up). The surface of PDMS should be protected from dust and contamination by applying scotch tape to its top surface. Following the same procedure, several PDMS replicas can be made from the same silicon master. Prior to binding the two PDMS layers, the inlet/outlet holes (access ports for fluid introduction) are pierced through the PDMS structures using a razor sharp stainless steel cutting tip (Harris Uni-Core Tip ID 1.0 mm).

The PDMS surface as cast is quite hydrophobic and does not stick to other surfaces. The most common method to reduce PDMS hydrophobicity and chemically activate its surface (to aid bonding) is to expose the targeted surface to oxygen plasma. The oxygen plasma treated PDMS surface forms permanent bonds upon contact with similarly cleaned silicon, glass or other PDMS surfaces. These surfaces should be brought into contact immediately because PDMS returns to its hydrophobic state in just a few minutes. We prepare our final two-layer microfluidic structure by permanently bonding the top and bottom PDMS layers. The surfaces to be bonded were treated in Diener plasma etch system (Diener Electronic, Jettingen, Germany) 50% O_2 for 12 seconds. Immediately afterwards, the two surfaces were aligned under the optical microscope and brought into contact in order to bond irreversibly (Fig. 2.15). The two-layered PDMS microfluidic structure is further cured at 80 °C (on a hot plate) for about 15 minutes to assist with the bonding.

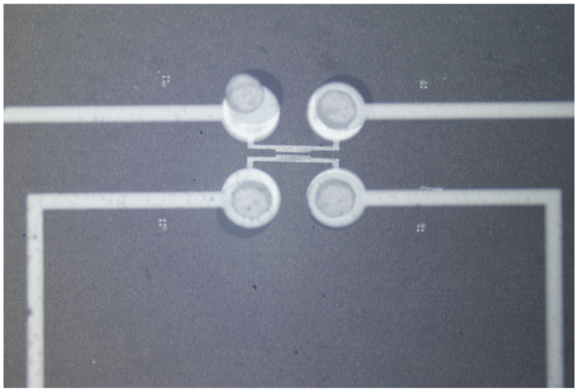

Figure 2.15 Optical microscope image of two aligned PDMS layers.

2.2.6 Final assembly of the nanofluidic device

In the final device, a two-layered PDMS structure is placed on top of the PMMA layer in alignment with the reservoirs as Fig. 2.16 demonstrates. Since the separation between the reservoirs is only 20 µm, the alignment of the PMMA and PDMS layers was performed under an optical microscope in conjunction with a micromanipulator.

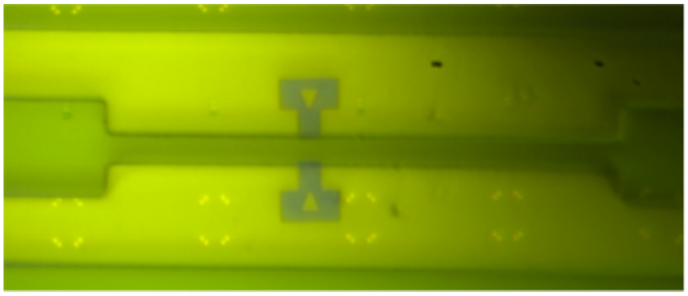

Figure 2.16 The alignment between the PDMS microfluidic structure and reservoirs patterned in PMMA.

Finally, standard silicon tubing was fixed to PDMS inlet/outlets using stainless steel connectors. The liquid was then pulled through the microfluidic channels to wet the reservoirs using two syringes, as shown in Fig. 2.17.

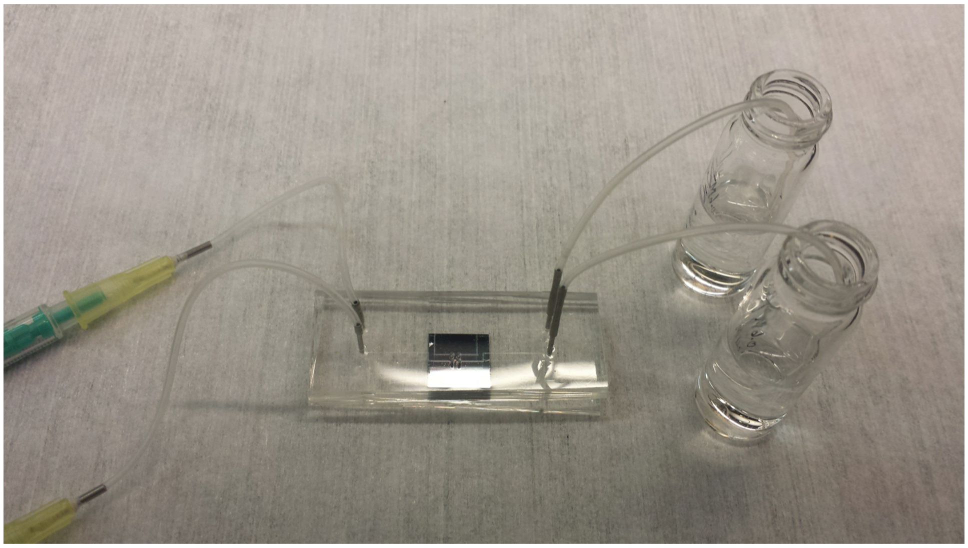

Figure 2.17 Final device assembly.

2.3 Measurement platform and experimental details

There was a measurable and stable ionic current moving through the nanotube instantly after adding the solution to both reservoirs and no current was seen during the control experiments on devices without CNTs. All of the solutions were unbuffered and had a pH of 6 (due to desolvation of ambient CO_2 DI water) unless noted otherwise. The ionic current-voltage relation (I-V curve) was recorded for bias values between ± 500 mV (100 mV increments), or up to the amplifier saturation point, and showed linearity for symmetrical solutions. Figure 2.18.a shows the recorded I-V curves in various concentrations of KCl electrolyte. Ionic conductance values calculated from the slope of the I-V curves are plotted in Fig. 2.18.b.

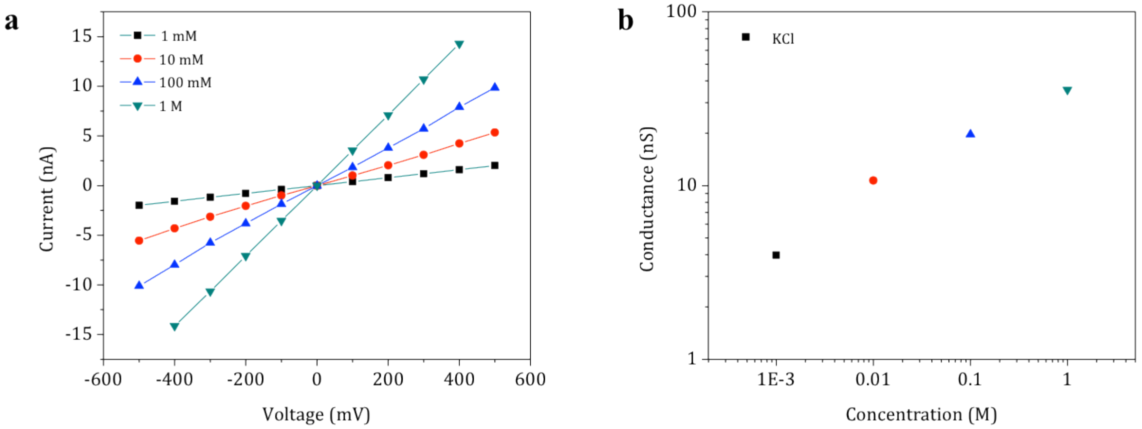

Figure 2.18 Electrical measurement of ionic current passing through individual CNT devices. a) Ionic current as a function of applied bias at various concentrations of KCl electrolyte. b) The calculated ionic conductance from I-V curves as a function of electrolyte concentration.

The electrical measurements were performed with sealed Ag/AgCl reference electrodes (BASi, MF-2078, 3.0 M NaCl), attached to an Axopatch 200B amplifier (Molecular Devices, Sunnyvale, CA) in the voltage-clamp configuration. The assembled device and the head stage were inside a Faraday cage. The temperature of the system was always in the range of 20-22 °C. All of the data plotting, analysis and fitting were performed using OriginPro 8 (OriginLab Corp., Northampton, MA).

We examine ion conduction through CNT devices by studying the effect of electrolyte concentration and composition on ionic conductance and reversal potential. Each experiment is performed on several devices to assure reproducibility of the results. The relative standard deviation (RSD%) associated with the data was estimated from three repetitions of conductance-concentration and reversal potential-concentration curves (see section 3.4) in KCl solution before proceeding with the rest of the experiments. Figure 2.19.a shows three repetitions of conductance-concentration curve and Figure 2.19.c shows three repetitions of reversal potential-concentration curves in a CNT device. The corresponding averaged graphs and standard deviation values are presented in Fig. 2.19.b and 2.19.d. The typical RSD% for conductance-concentration and reversal potential-concentration curves are ~ 7 % and ~ 3 %, respectively.

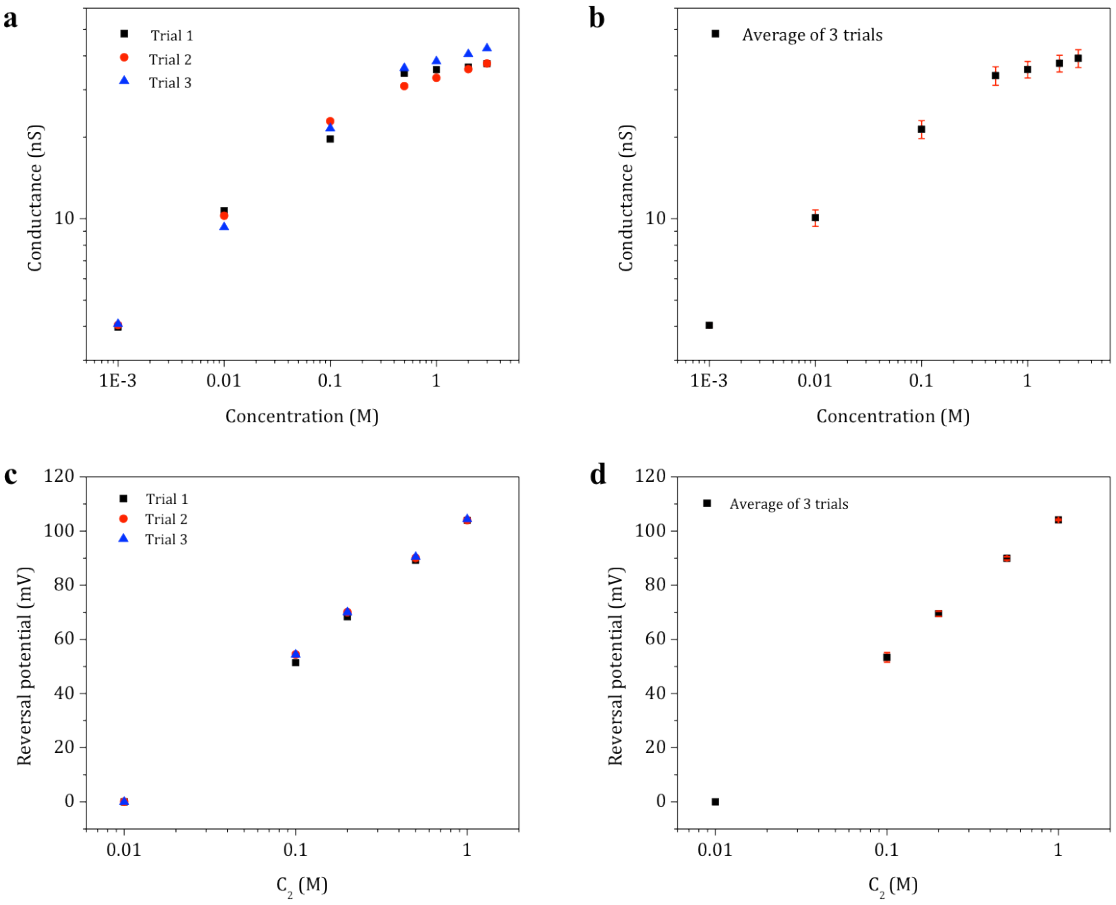

Figure 2.19 Three repetitions of conductance-concentration (a) and reversal potential-concentration (c) curves in KCl solution. The corresponding averaged graphs and standard deviation bars (red) are presented in panel (b) and (d).

CHAPTER 3

Ion Conduction in Carbon Nanotubes

Selectivity and Permeability

3.1 Introduction

In studying biological channels, ion permeation is commonly regarded as a barrier-hopping process to explain channel selectivity and conduction characteristics [59]. Hydrated ions often have to overcome appreciable free-energy barriers when moving through narrow hydrophobic pores because of geometric constraint and/or complex energetic interplay among ions, water molecules and nanopores [59, 83].

Transferring a fully-hydrated ion from bulk into a confined nanopore is associated with both entropic and energetic penalties [59, 84]. Ions in bulk phase are surrounded by locally-structured and tightly-bound water molecules (hydration shells) that can be characterized by the radial distribution of water molecules around ions [117]. A solvated ion has to strip off, or rearrange, some of the water molecules in its hydration complex in order to enter a pore with radial dimensions comparable or smaller than its hydrated radius [59, 118].

In biological ion channels, ions of different types often encounter distinct free energy barriers, originated from ion interaction with the pore [59]. Subtle differences in barrier height and profile can lead to remarkable variation in the permeation properties of comparable ions [59]. For instance, calculations based on transition-state theory have predicted that a permeability ratio of 100-1,000 for K^+ over the smaller ion Na^+ in potassium channels is obtained from a free energy barrier difference of only ~ 3.5 Kcal/mol, which is a small fraction of the ions' enthalpy of hydration [119]. Additionally, in the case of the CaK channel, it is able to finely discriminate between K^+ and its analogues, Ti^+, Rb^+ and NH_4^+ [120].

Molecular dynamics simulations have repeatedly demonstrated that free energy barriers imposed on ions traveling through nanopores are not exclusive to biological ion channels and are observed in other types of confined hydrophobic nanopores including SWCNTs [77, 83, 84]. Many atomic simulations demonstrated that small ions such as K^+, Na^+ and Cl^- encounter distinct energy barriers upon entering sub-nanometer SWCNTs; this phenomenon can lead to intrinsic ion selectivity [77, 83, 84, 121, 122]. The water molecules, on the other hand, seem to enter at no cost [35, 123].

The barriers mainly arise because ions have to shed off some of their associated water molecules in their first and most strongly-bound hydration shell in order to be accommodated by the pore [77, 83, 84]. The results of these simulations also suggest that the energy barriers mainly exist at the entrance and exit of these pores (i.e. ion movement along the pore is almost frictionless) [45, 77, 123]. It has been demonstrated that barrier heights are closely correlated to the pore effective size and ion properties related to hydration (e.g. hydrated radius and hydration strength) [77, 123, 124].

Translocating ions in wider SWCNTs (i.e. diameters ≥ 1.0 nm), on the other hand, preserve their innermost hydration shells and their bulk coordination number almost completely [77]. The structural order of ion hydration shells (i.e. orientation of water molecules within the shell) may still be significantly distorted [125, 126]. The energy barriers imposed on ions by SWCNTs in this diameter range are much smaller and mainly originate from the instability and structural rearrangement of the hydration shells as well as the loss of more outlying water molecules [118, 125, 127].

Favorable interactions between ions and nanopore can somewhat compensate the energy cost of overcoming permeation barriers [79]. Molecular dynamics simulations have shown that the presence of fixed charges on the pore and/or external electric field along the tube axis facilitates the ion entry into the pore and elevates the ion occupancy inside the channel [79]. Electrostatic interactions between ions and charged (or polar) moieties of the channel functionalities are one of the major mechanisms through which biological ion channels achieve cationic or anionic selectivity (i.e. higher selectivity towards counter-ions over co-ions) [59]. Simulation studies have predicted similar results and conclusions for ion permeation through narrow SWCNTs [45, 78, 79, 81].

3.2 Cation selectivity

The electrostatic environment created by fixed charges at the pore entrance achieves selectivity between anions and cations in many protein ion channels [86]. In most cases, channels are selective towards ions carrying the opposite charge of the channel entrance region. Cation selective ion channels, such as CaK [87], nicotinic acetylcholine receptor (AChR) [128] and ryanodine receptor (RyR) [129] channels, and anion selective channels, such as cystic fibrosis transmembrane conductance regulator chloride (CFTR) [130] and glycine receptor chloride (GlyR) [131] channels, support such a selectivity mechanism. Here, we first show that our CNT devices are highly selective towards cations and later provide evidence that this behavior is most likely due to the negatively charged carboxyl groups present at the nanotube rim atoms.

Examining the relationship between ionic conductance and the monovalent equivalent of electrolyte concentration (i.e. concentration of ML_3 salt is multiplied by a factor of three when comparing to ML salt) for a series of electrolytes with varying ion sizes shows that CNTs are highly cation selective (Fig. 3.1.a). While conductance does not vary appreciably if chloride ions are replaced by larger and less mobile anions, such as hexacyanoferrate (III), it decreases significantly if potassium ions are exchanged with much larger cations, like tris(bipyridine)ruthenium (II). These results indicate that cations are the main charge carriers through the CNT devices. Fig. 3.1.b shows the results of similar experiment on a leakage device. Both reduction and rectification of ionic current due to ionic hinderance have been previously reported for CNTs with small diameters [34, 132].

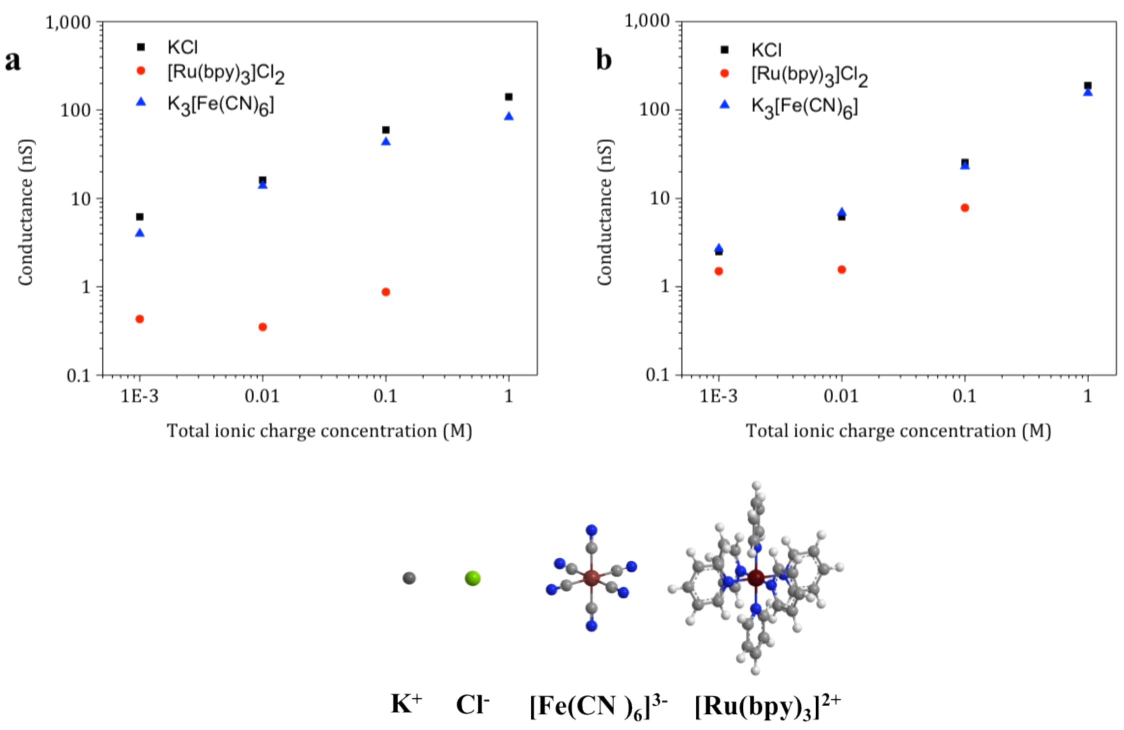

Figure 3.1 Effect of ion size on conductance. Ionic conductance is plotted as a function of total ionic charge concentration for electrolytes with varying ion sizes. a) Comparing the conductance-concentration curves of KCl (black squares), $K_3[Fe(CN)_6]$ (blue triangles) and $[Ru(bpy)_3]Cl_2$ (red circles) suggests that cations are the major charge carriers through carbon nanotubes. b) Results of a similar experiment performed in a leakage device.

3.3 Relative permeability of cations over anions

The Nernst equation allows for the determination of the equilibrium potential for a specific ion if the concentrations across the membrane are known [133]. However, the plasma membrane in the living cells is often permeable to more than one type of ion. This results in the resting membrane potential (zero current potential) to be established at a value rather than the equilibrium potential for any of the contributing ions [59]. The Goldman–Hodgkin–Katz (GHK) equation allows us to calculate the membrane potential (E_{rev}) from the relative contribution of permeable ions (i.e. concentration gradient and relative membrane permeability of each ion) [134, 135]. For instance, if a plasma membrane is permeable to K^+, Na^+ and Cl^-, the GHK equation is written as [59]:

$$E_{rev} = \frac{RT}{F}\ln\left(\frac{p_K\,[K^+]_{cis} + p_{Na}\,[Na^+]_{cis} + p_{Cl}\,[Cl^-]_{trans}}{p_K\,[K^+]_{trans} + p_{Na}\,[Na^+]_{trans} + p_{Cl}\,[Cl^-]_{cis}}\right) \qquad (3.1)$$

Where p_i and $[i]$ are the relative membrane permeability and concentration of the ion, *i*; and R, T and F have their usual thermodynamic meanings.

We performed reversal potential measurements to quantify the permeability ratio of cations over anions (P_c/P_a) through our CNT devices according to the GHK formulation. In this experiment, the electrolyte concentration was fixed to 10 mM in one reservoir (C_1) and was gradually increased in the other from 10 mM to 3.0 M (C_2). Ions move from the concentrated solution (high chemical potential) to the diluted one (low chemical potential) in the manner consistent with the channels' selectivity. The reversal potential (the potential at which there is no net current) was measured a few minutes after the solutions were set up.

Representative graphs of reversal potentials (calculated as the potential of the diluted side less the potential of the concentrated side) at each value of C_2 are shown in Fig. 3.2.a.

The permeability ratio of cations over anions (P_c/P_a) in KCl is computed as 100 ± 8 according to the GHK formulation [59, 134-136]. The recorded reversal potential at each value of C_2 was always positive on the more dilute side, which is consistent with the cation selectivity assumption of these channels.

The permeability ratio of cations over anions in a leakage device was similarly measured and calculated as ~ 5 ± 1 (Fig. 3.2.b). The slight cation selectivity of leakage devices is perhaps due to the ionizable functionalities on the surface of PDMS and oxygen plasma treated PMMA.

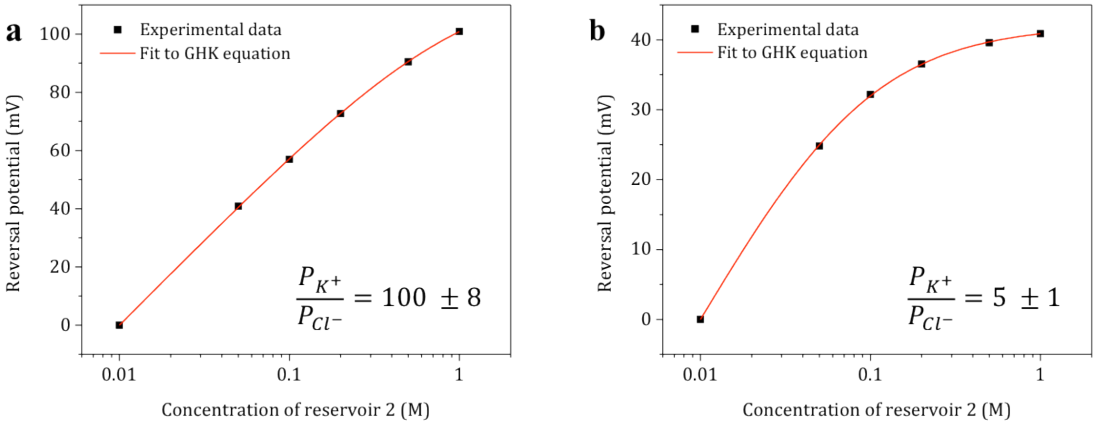

Figure 3.2 Reversal potential as a function of KCl concentration in reservoir 2. Concentration of KCl in reservoir 1 was fixed at 10 mM and was varied between 10 mM and 1.0 M in reservoir 2. Reversal potential was always positive on the more dilute side confirming the cation selectivity of these channels. a) CNT device, the solid line is the best fit of data according to GHK equation (Adj. $R^2 = 0.999$) yielding a permeability ratio of 100 ± 8 between cations and anions. b) Results of a similar experiment performed in a leakage device yield a permeability ratio of 5 ± 1.

High cation selectivity of CNTs strongly suggests that the nanotube possesses fixed negative charges. In Chapter 4, we discuss the results of the experiments designed to identify the nature and location of pore negative charges.

3.4 Permeability of K^+-like cations

Here we demonstrate that CNTs are able to intrinsically differentiate among K^+-like ions. We do this by comparing the conductance of KNO_3, NH_4NO_3 and $TlNO_3$ electrolytes (with pH ~ 6) at various concentrations (Fig. 3.3.a). Without considering the energetics of permeation, K^+, NH_4^+, and Tl^+ are expected to demonstrate very similar permeation properties. NH_4^+ (Tl^+) only differ by ~ 11% (8%), 0% (0 %) and 0% (2%) in crystal radii, hydrated radii and bulk mobility, respectively, from K^+ [137, 138]. For all concentrations studied, the conductivity decreases with hydration enthalpy of the associated cations in bulk. The cations with looser water molecules in their hydration shells exhibit higher conductivity [139], which is possibly reflecting the energetically costly changes in hydration state during permeation. Transformation of water-ion complex in ion permeation through CNTs is reported by several MD simulation studies [77, 84, 124]. In the similar experiment, the leakage device conductance did not show any obvious dependence on the cation type (Fig. 3.3.b).

These results offer strong evidence to demonstrate that there are other specific factors dictating the energetics of ion transport besides bare-radius and mobility. In particular, interactions between water molecules and ions, not accounted for in continuum theory-based models, should not be overlooked.

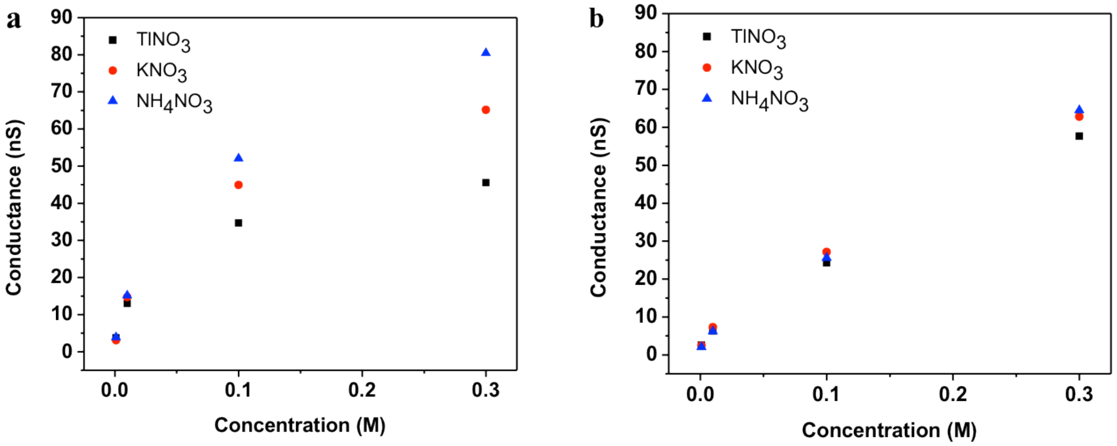

Figure 3.3 Effect of cations enthalpy of hydration. Conductance dependence on KNO_3 (red circles), NH_4NO_3 (blue triangles) or $TlNO_3$ (black squares) concentration was measured. The pH of 10 mM, 100 mM and 300 mM NH_4NO_3 solutions were adjusted to ~ 6.0 using 2 mM citric acid buffer system. a) CNT device, cations with looser water molecules in their hydration shell exhibit higher conductance. b) Results of a similar experiment performed in a leakage device.

3.5 Conductance saturation

In studying biological channels, ionic current/conductance often reaches saturation as the concentration of permeating ions is increased [59]. Figure 3.4 shows the conductance dependence on permeating ion activity in CFTR channels [140] and gramicidin A channels [141]. At low ionic strengths conductance strongly depends on ion concentration, but it gradually saturates following a Michaelis-Menten profile. Conductance-concentration curves obtained from our CNT devices, also exhibit a saturation effect in a Michaelis-Menten form: $G = G_{max}/(1 + K_m/[K^+])$, G_{max} = 161.1 ± 9.3, K_m = 0.17 ± 0.03 (Fig. 3.5).

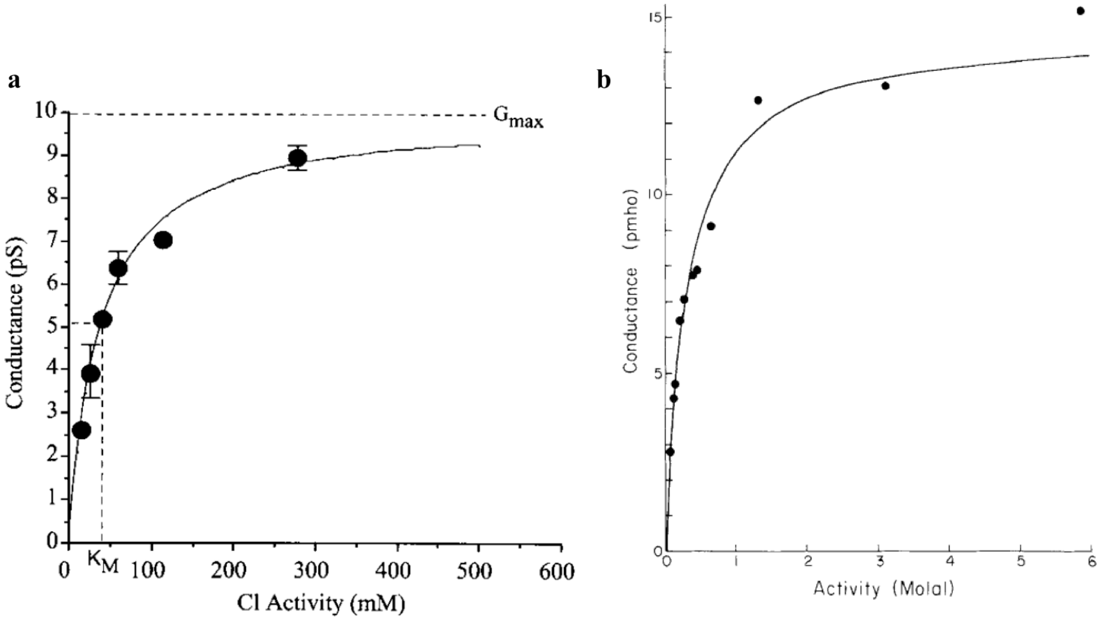

Figure 3.4 Single-channel conductance as a function of permeating ion activity. a) CFTR conductance as a function of bilateral Cl^- activity. Solid line is the best fit of data according to Michaelis-Menten relation with K_m = 37.6 mM and G_{max} = 10.0 pS. Adapted in part from ref. [140], b) Gramicidin A conductance as a function of Na^+ activity. Solid

line is the best fit of data according to Michaelis-Menten relation with K_m = 0.31 m and G_{max} = 14.6 pmho. Adapted in part from ref. [141].

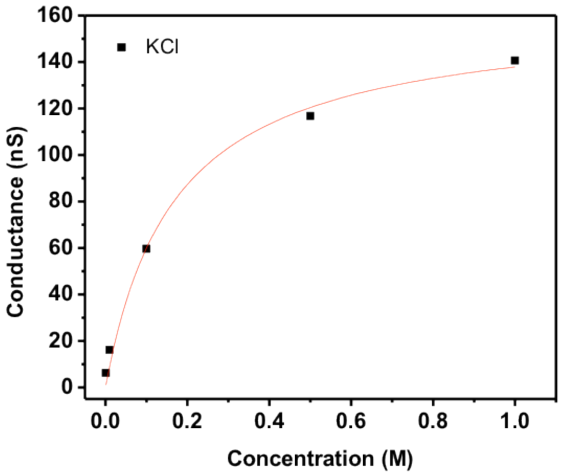

Figure 3.5 CNT conductance dependence on KCl concentration. The best fit of Michaelis-Menten equation with half-saturation point K_m = 0.17±0.03 and maximum conductance G_{max} = 161.1±9.3 is plotted as a solid line. (Adj. R-Square: 0.991)

This Michaelis-Menten relationship suggests that the permeation process involves both concentration-dependent and concentration-independent steps [45, 59, 142]. At low concentrations, conductance depends on ions to diffuse in the solution and find the channel mouth, a process which becomes faster as ion concentration increases. This reliance results in a strong dependence of conductance on ion concentration at low concentration range. Once there are plenty of ions present at the pore mouth, the conduction process is limited by the time each ion takes to pass through the channel. In this regime, ions must wait for the preceding ones to overcome free energy barriers and translocate through the pore. Since every ion takes a finite amount of time to pass the barriers, the overall permeation process does not get any faster by raising the concentration and as a result conductance saturation is observed.

Conductance-concentration profiles obeying a Michaelis-Menten relationship have been seen among the results of atomic simulations of ion conduction in narrow SWCNTs. T. A. Hilder and coworkers designed and studied a highly anion-selective CNT-based nanopore, 4.53 Å in effective diameter and 34 Å in length, with terminated polar carbonyl groups embedded in a lipid bilayer [45]. They observed that ions are conducted through a knock-on mechanism, meaning that the outermost ion is ejected from the pore through repulsive forces as a new ion enters the pore. In addition, ions have to overcome two large energy barriers located at both ends of the nanopore. They observed that ions enter the nanotube faster as electrolyte concentration increases; however, the time they take to exit the pore does not change. In other words, at high concentrations, overcoming the free energy barrier near the nanotube exit becomes the rate-limiting step in ion conduction. The current-concentration curve, studied by T. A. Hilder et al., followed a Michaelis-Menten profile.

3.6 Permeability of alkali metal chloride series

Subtle differences in interaction energies between hydrated ions and biological ion channels can lead to remarkable selectivity differences towards comparable ions, such as alkali metal cations [59]. No universal model has yet been proposed to explain the ion selectivity across the nanopores, since the origin of selectivity is quite complicated and involves more factors than the relative diameter and charge of the ions and pore [59].

For the sake of comparison, we measured the conductance of our CNT devices as a function of electrolyte concentration in symmetrical aqueous solutions of alkali metal chlorides. As shown in Fig. 3.6.a, channel conductance across the series is non-intuitive and does not follow any particular trend, such as ion mobility, radius or even enthalpy of hydration [137-139]. Across all of the tested devices, conductance increases from LiCl to KCl and then subsequently declines for the remainder of the cations in the series. One simple explanation could be that cations are getting larger in size from Li^+ to Cs^+; so perhaps at some critical diameter, steric effects begin playing a role and changing the energetics of ion permeation steps. We view this as unlikely, as there is only a very slight difference between each of the bare radii and each of the hydrated radii of K^+, Rb^+ and Cs^+ cations. Figure 3.6.b shows conductance dependence on concentration of alkali metal chloride series in a leakage device.

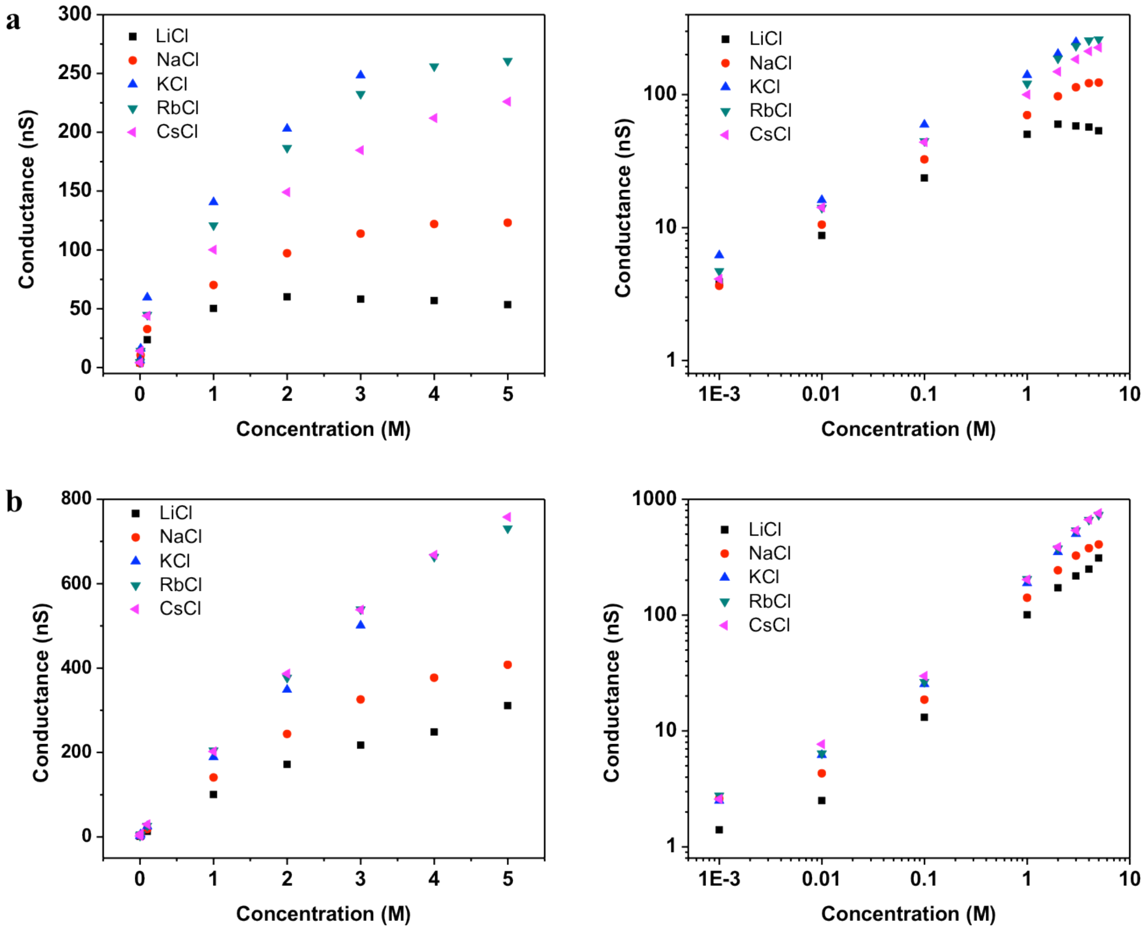

Figure 3.6 Conductance-concentration profiles recorded in symmetrical solutions of alkali metal chlorides, in linear and double logarithmic scale. a) CNT device. b) Leakage device.

Another explanation for the observed trend is that there are differences in radial distribution and structure of ions and water molecules in channels under confinement [84]. In narrow hydrophobic pores, ions may move differently along the pore depending on their radial localization, and therefore experience different friction forces in the pore [143]. Ions may also shift their radial distribution and reorganize their hydration shells in order to facilitate the process of passing the counter-ions along the way [84]. The differences in cation radial distribution in narrow CNTs could be another possible explanation for the observed conductance trend in alkali metal chlorides.

Conductance comparison of alkali metal chloride series highlights the complexities of ion permeation through carbon nanotubes and the importance of further studies in order to better elucidate and separate the overall free energies of ion transport into individual contributions of involved factors.

CHAPTER 4

Effect of Pore Surface Charges on Ion Conduction through Carbon Nanotubes

4.1 Introduction

In this study we experimentally investigate ion permeation in individual carbon nanotubes and demonstrate that, in addition to structural similarities, ion conduction in CNTs shares many common characteristics with biological ion-selective channels. In particular, there is substantial evidence that ionic conductance and blockade of both carbon nanotubes and protein ion channel are strongly influenced by the presence of fixed charges around the pore entrance [86].

For the protein pore, even in the absence of structural information, the effect of entrance charges has been extensively studied through experimental manipulation of the surface electrostatics, such as by changing the ionic strength, composition or pH of the bath solutions or by chemical modification of the protein using group specific reagents or site-directed mutagenesis [86]. Here, we perform similar studies of the deprotonated carboxyl groups present at the CNTs' entrance to show similar effects on ion permeation.

4.2 Location of pore charges

For protein ion channels, experimental manipulation of surface electrostatics on channel properties is a powerful tool to probe the nature and location of surface charges [86]. For example, the extracellular application of the carboxyl-specific reagent, trimethyloxonium, to the CaK channel reduces channel conductance by removing the electrostatic potential contributed by carboxyl groups at the channel entrance, an effect that is largest at low ionic strengths [87]. For the RyR channel, the introduction of large polycations like neomycin blocks pore conduction, indicating the presence of negatively charged groups on both channel ends [144].

In order to show that negative surface charges affecting the transport through CNTs are localized at the nanotube entrance, and not along its core as proposed by S. Lindsay group [132], we studied the effects of surface charge modification on reversal potential, following the methodology and arguments of N.R. Scruggs and coworkers [145]. They designed a series of experiments to show how modifying the localized charge density at the entrance of multi-walled carbon nanotubes can strongly influence the transport of electrolytes through these channels. They altered the surface potential using either electrolyte screening or electrostatic adsorption of positively charged polymers on the MWCNT entrance. The MWCNTs serving as fluidic channels in their study were 15-65 nm in inner diameter and embedded in a 1μm-thick polystyrene membrane.

Similar results were obtained when we subjected our individual CNTs with much smaller diameters (≤ 1.5 nm) to the same experiment. First, we measured the reversal potential as the concentration of KCl solutions across the nanotube was decreased. The ratio between the two concentrations was always fixed at 2:1 in order to maintain a constant diffusional current. The results, presented in Fig. 4.1.a, demonstrate that reversal potential sharply increases (in absolute value) as KCl concentration drops until it eventually levels off at low concentrations (≤ 1 mM). This behavior is expected in the presence of fixed charges on the two ends of the nanotube establishing two electric potentials known as Donnan potentials [146, 147], which contribute to the reversal potential. Increasing the KCl concentration (and, consequently, the ionic strength) screens the surface charges and reduces the magnitude of Donnan potentials.

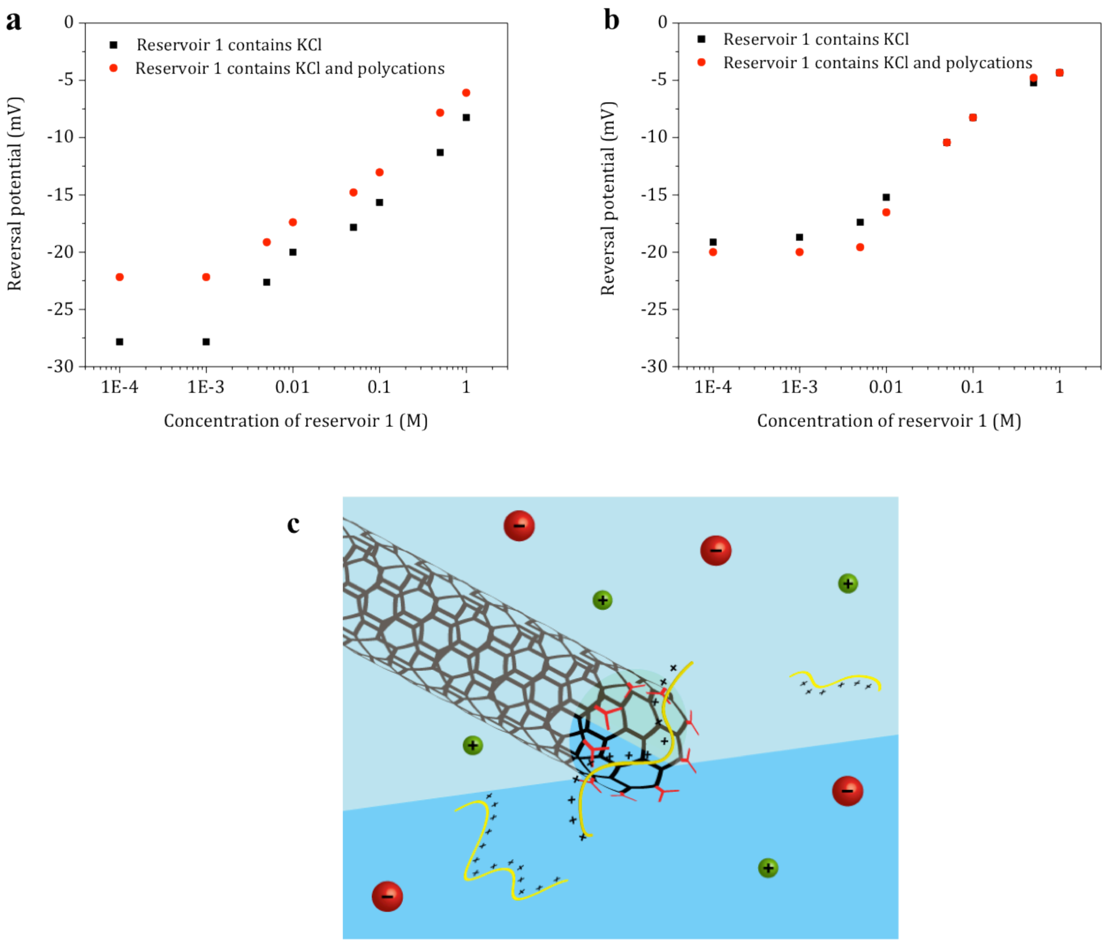

Figure 4.1 Probing the location of pore surface charges. Reversal potential recorded as we modulated the negative surface potentials using electrolyte screening or electrostatic adsorption of polycations. The KCl concentration in reservoir 2 was always equal to 2 times the concentration of reservoir 1. Black squares: reversal potential as a function of KCl concentration in reservoir 1. Red circles: reversal potential as a function of KCl concentration in reservoir 1 after addition of a small amount of polycation to reservoir 1. a) CNT device, b) leakage device, c) cartoon representation of polycation adsorption on the negatively charged carboxyl groups at nanotube entrance.

Similar measurements were performed with a polycation solution, poly(dimethylamine-co-epichlorohydrin-co-ethylenediamine) with average M_W ~ 75,000 and final concentration of 20 μg/ml, added to one reservoir (Fig. 4.1.a). While the positively charged polymers are too large to pass through the nanotube their electrostatic adsorption onto the negatively charged CNT mouth modulates the Donnan potential on that end (Fig. 4.1.c). At a low ionic strength, the addition of polycations causes a considerable upward shift in reversal potential; however, the effect is progressively smaller with increasing ionic strength as surface charges are effectively screened.

The results of the similar experiments performed on a leakage device are presented in Fig. 1.4.b. Similar to CNT devices, the reversal potential increases in absolute value as the reservoir concentrations decrease. However, it plateaus at smaller reversal potential values (-20 mV) and at higher concentrations ~ 10 mM. This suggests that the effect of surface charges in a leakage device is smaller than in the CNT devices. Additionally, the presence of polycations in the solution has a very small effect on the magnitude of the reversal potential.

Lastly, we performed a control experiment using polyanions to eliminate the possibility of non-specific adsorption of polymers onto the nanotube entrance. Instant rectification of ionic current (I-V), with symmetrical 100 mM KCl solutions in both reservoirs occurred when the same small amount of the polycation solution was added to one of the reservoirs (Fig. 4.2.a). Substituting the polycation with a polyanion, poly(sodium 4-styrenesulfonate) with M_W ~ 70,000 and 20 μg/ml concentration caused almost no change in I-V characteristics, eliminating the possibility of nonspecific adsorption of polymers onto the nanotube. The addition of polymers to leakage devices did not cause any significant change in their I-V characteristics (Fig. 4.2.b). These results highlight the influence of ionized carboxyl groups at the CNT entrance on ionic conductivity of these channels.

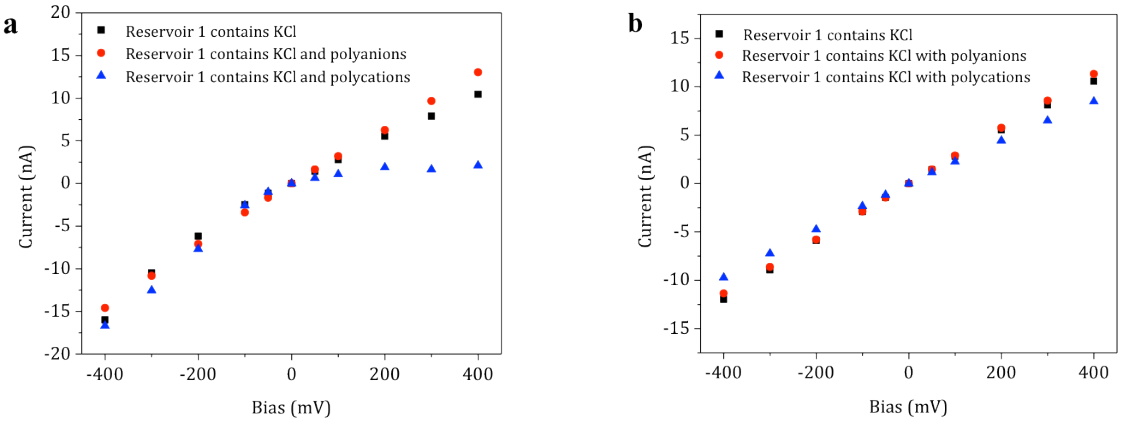

Figure 4.2 Rectification of ionic current upon addition of a polycation solution to reservoir 1 (non-grounded). All current-voltage curves were generated at 100 mM KCl ionic concentrations. Squares: Initial KCl solutions on both sides. Circles: Polyanion: Poly(sodium 4-styrenesulfonate) with M_W ~ 70,000 and 20μg/ml concentration, was added to reservoir 1 (non-grounded). Triangles: Polycation: Poly(dimethylamine-*co*-epichlorohydrin-*co*-ethylenediamine) with average M_W ~ 75,000 and 20μg/ml, was added to reservoir 1.

4.3 Nature of pore charges

Subsequent study of conductance as a function of pH provides evidence on the chemical nature of surface charges. The recorded conductance of 100 mM KCl in the pH range of 2.0 - 8.0 is suggestive of a simple titration curve (Fig. 4.3.a). The conductance is nearly constant at more basic pHs, titrates away sharply by lowering the pH and remains about ~ 15 % of its initial value at more acidic pHs. The data are well fit by a single proton dissociation curve with a pK_a of 4.8 ± 0.1, which closely matches the reported pK_a value of 4.5 for carboxylate groups at the cut ends of CNT in aqueous solutions (Fig. 4.3.c) [148]. F. Fornasiero et al. also reported a pKa of 4.8 for the functional groups, most probably carboxylates, governing the ion rejection through 0.8-2.6 nm wide CNT membranes under a pressure-driven flow [28]. Other groups have also reported reduction in ionic current through individuals or large collections of carbon nanotubes at low pH values [33, 34, 41]. Stochastic pore-blocking transport phenomena (i.e. cations obstructing the enhanced proton transport inside the pore) as reported by M. Strano group have never been observed in any of our measurements [56]. The conductance dependence on pH in leakage devices is consistent with presence of silanol groups on the channel walls (Fig. 4.3.b) [149].

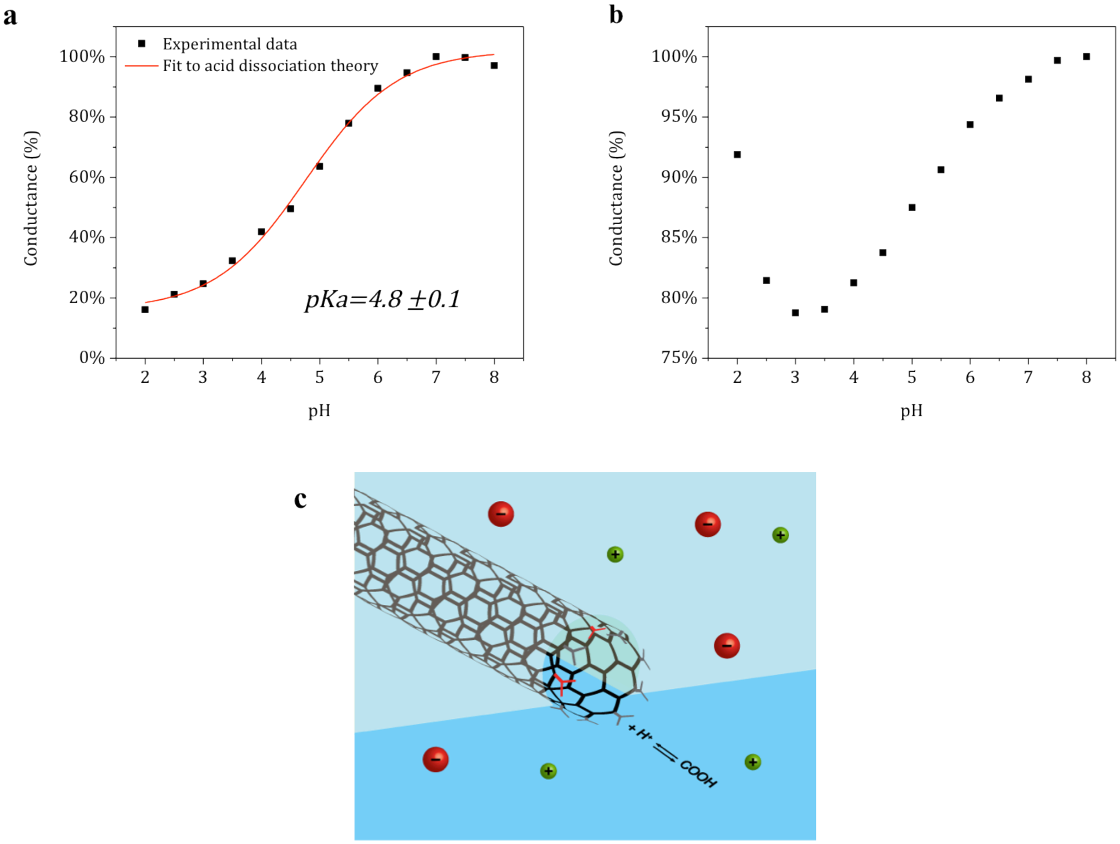

Figure 4.3 Identifying the chemical nature of pore surface charges. Conductance variation, with respect to the solution with pH = 7.0, recorded as we symmetrically reduced the pH of 100 mM KCl solutions from 8.0 to 2.0. Solutions prepared for studying the effect of pH modulation on ionic conductance contained 100 mM KCl and 2 mM of buffering agents: citric acid (for pH 2.0 - 6.0) and phosphoric acid (for pH 6.5 - 8.0). a) CNT device, the solid line is the best fit of data based on simple monoprotic acid dissociation theory (Adj. $R^2 = 0.995$) yielding a pK_a of 4.8 ± 0.1 for surface functional groups. b) Leakage device, the conductance dependence on pH is consistent with the presence of silanol group on channel walls. c) Protonation of carboxyl groups located at the nanotube entrance removes the surface charge effects.

The observed strong pH dependence of channel conductance highlights the significance of the protonation state of carboxyl groups at CNT ends and the local electric potentials created by these groups. At basic pHs, the deprotonated carboxyl groups attract the cations into the pore, which leads to high current levels through mechanisms like electroosmotic flow, see section 1.2.2. It has been shown both through experiments and MD simulations that electroosmotic current is not exclusive to channels with charged walls and can be generated even inside the neutral nanochannels based on the differences in cross-sectional distribution and movement of ions in the channel [150-152]. Once the carboxylate groups are fully protonated and the negative surface charges near the pore mouth are removed, conductance drops to extremely low values.

Another important implication of these results is that other charges beside the carboxyl groups (e.g. amphoteric silanols residing on the surface of SiO_2 substrate or possibly existing charges along the nanotube core) do not seem to play a significant role in the ion permeation process. The presence and influence of carboxyl groups at the cut ends of CNTs is often disregarded when theoretical models are proposed to explain the experimental data. It is also worth mentioning that carboxyl groups provide a useful knob for controlling ionic current through these channels without scarifying the smooth interior of the nanotube.

4.4 Conductance dependence on ionic strength

4.4.1 Introduction

Understanding the relationship between conductance and concentration in pore structures is important because it contains valuable information on the conduction mechanism. Continuum mechanics has been a powerful theory to describe and predict fluid behavior in macro- and microfluidics systems. In nanofluidics, channel height becomes comparable to the thickness of the electrical double layer or even molecular dimensions [26]. In this regime, intra-molecular interactions between fluid molecules and channel walls become critically important and may lead to deviations from the continuum hypothesis [26, 153]. Additionally, at these length scales macro parameters such as density, viscosity and velocity may no longer vary continuously over the range of molecular mean free paths and relaxation times [154-156]. More importantly, continuum-based descriptions do not consider molecular nature, short-range interactions and confinement effects, despite numerous reports on their significance [83, 157]. Based on these limitations, several groups proposed 2-5 nm as the length scale below which continuum theory tends to break down [1, 156-158], although a universal agreement over the exact length scale has not yet been reached.

All-atom MD simulations take detailed atomic structures and interactions among pore, ions and water molecules into account and as a result, have been utilized extensively over the last few years to obtain explicit information on ion transport across both biological and synthetic nanopores [153, 159]. Comparing experimental results to simulation observations remains challenging because even simulating extremely short pores and reaching the time scales necessary to extract accurate information on ionic current is excessively time consuming and costly [160, 161]. Moreover, the results of MD simulations are often highly dependent on the chosen molecular force field and whether computationally demanding parameters, such as polarization and flexibility, are taken into account [84, 162].

Previous studies have shown that the ionic conductance of narrow CNTs is much larger than what classical descriptions predict for a pore with similar geometry [41]. In addition, CNT conductance exhibits a power-law dependence (i.e. linear in double-logarithmic scale with estimated slope of ~ 0.4) on KCl concentration in the range of 1 mM-1.0 M [41]. These characteristics were explained through continuum theory by applying the Poisson-Nernst-Planck-Stokes equations [132]. The proposed model assumed that a large negative charge resides along the nanotube wall; consequently, the solution inside the channel becomes cation rich and generates large electroosmotic currents in the presence of an applied electric field.

In this work we take a different approach to explain the conductance-concentration relationship observed in narrow CNTs, which accounts for the inevitable role of ionized carboxylates at the pore entrance on ionic transport. We use this approach because similar conductance-concentration relations (square root dependence of conductance on concentration) have been observed in some biological transmembrane proteins through which the ion transport mechanism experiences a local electrostatic potential at the channel entrance, such as certain types of inward-rectifying potassium channels [163], hemolysin channels [164] and porins [165].

4.4.2 Description of the proposed model

In biological channels, square root dependence of conductance on concentration is expected if the local concentration of current-carrying counter-ions near the pore mouth is increased through electrostatic interactions [164-169]. At low ionic strengths, a large surface potential raises the counter-ion concentration near the channel entrance. As the ionic strength is increased, these surface potentials are screened and the local concentration of counter-ions is buffered. Conductance rapidly increases with concentration at low ionic strengths while it only slightly varies near the maximum conductance of the channel. For instance, succinylation of neutral porins (i.e. introducing fixed negative charges at the channel mouth) reduces the slope of the conductance-concentration curve on a double-logarithmic graph from ~ 1 to 0.5 (Fig. 4.4) [166].

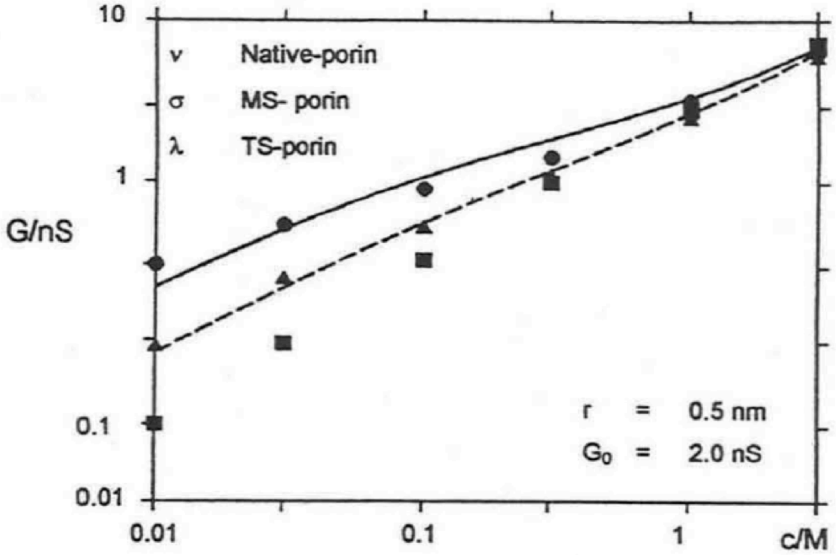

Figure 4.4 Single-channel conductance of native (filled squares), mono/di-succinylated porin (filled triangles) and tetra-succinylated porin (filled circles) as a function of KCl

concentration. The solid line is the best fit of data according to equations (4.1) to (4.3) assuming the channel radius and localized charge at channel mouth are 0.5 nm and -1.0 ē, respectively. The dash line is a similar fit assuming the same channel radius and -0.6 ē. The conductance of native porin (neutral channel mouth) is a linear function of KCl concentration. Adapted from ref. [166]

For protein ion channels, a simple electrostatic model based on the Gouy-Chapman theory of the electrical double layer is used to find the conductance as a function of concentration. This is measured by calculating the local concentration of counter-ions near the channel entrance as a function of bulk concentration and surface potential at the channel entrance [170-172]. The channel conductance is then determined by the local concentration of permeant ions at the channel mouth.

In this model, ions in the bulk phase see the negatively charged groups at the channel entrance as an effective point charge, q, which establishes a negative surface potential, Φ. This local potential gives rise to the buildup of an electrical double layer, or a counter-ion cloud at the channel mouth, which ultimately leads to the channels' overall selectivity, cation over anion and multivalent over monovalent.

The surface potential dependence on bulk ionic strength and pore radius, r, can be estimated from the Gouy-Chapman theory as follows:

$$\Phi = \left[\frac{q}{4\pi\varepsilon_0\varepsilon r}\right] . e^{\frac{-r}{\lambda_D}} \tag{4.1}$$

Debye length, λ_D, is a parameter that determines how far the electrostatic potentials are extended in the solution and depends on the ionic strength of the electrolyte; ε_o and ε are the absolute dielectric constant of free space and the relative dielectric constant of water, respectively.

When the channel radius is smaller than the Debye length, the concentration of cations near the channel mouth is larger than that in the bulk. This elevated concentration at the pore entrance, C^+_{local}, can be obtained from the Boltzmann distribution:

$$C^+_{local} = C^+_{bulk} \cdot e^{\left[\frac{-z\Phi F}{RT}\right]} \tag{4.2}$$

where C_{bulk} is the ion's bulk concentration, z is the charge on the ion and R, T, and F have their standard thermodynamic significance.

Total conductance, G (C), can now be written as the product of molar conductivity, G_{molar}, and the local cation concentration at the pore mouth:

$$G\,(C) = G_{molar} \cdot C^+_{local} \tag{4.3}$$

Figure 4.5.a shows plots of CNT conductance in LiCl, NaCl and KCl electrolytes over the range of 10 mM to 2.0 M in a double-logarithmic scale. Although the observed conductance values depend on the electrolyte type, the shapes of the conductance-

concentration curves are identical for all three salts. When this same model (Fig. 4.5.b) is applied to CNT, the fits shown in Fig. 4.5.a are obtained if the channel effective radius and number of elementary charges present at the channel mouth are assumed to be ~ 0.5 nm and ~ 2.6 ē, respectively. The results of the fit are presented in Table 4.1. These values are reasonable for CNT devices and fairly consistent across all three electrolytes tested. These results are expected since channel radius and surface charges are basic properties of the nanopore and should not vary by the nature of the electrolyte.

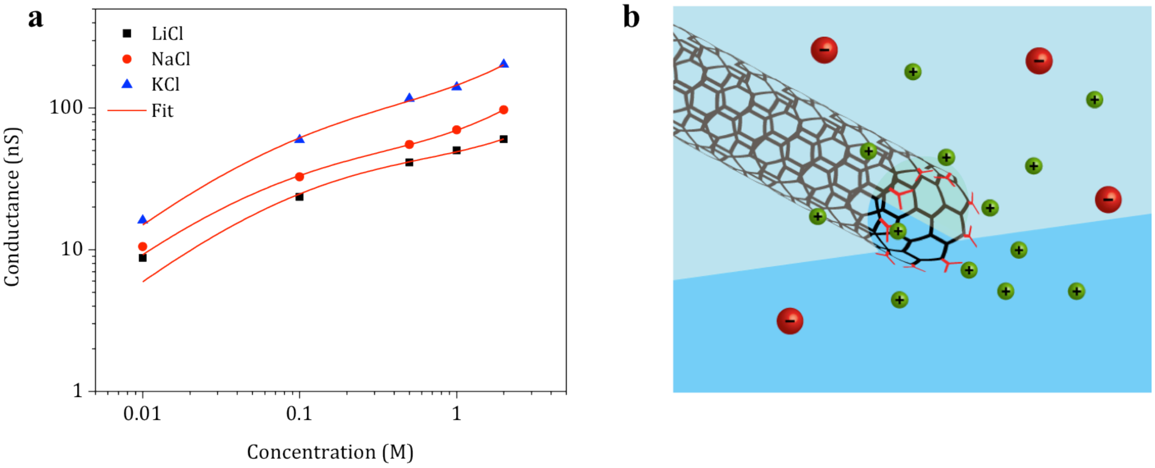

Figure 4.5 Proposing an electrostatic model, based on the Gouy-Chapman theory, to explain ion conduction through CNTs. a) Ionic conductance dependence on concentration of LiCl (black squares), NaCl (red circles) and KCl (blue triangles) electrolytes, in low and medium concentration range. Solid lines are the best fit of data (Adj. $R^2 = 0.99$) based on the equations (4.1) to (4.3). b) Cartoon representation of the electrostatic mechanism through which ion permeation in CNTs is explained in this work. In this model, the negative surface potential created by the deprotonated carboxyl groups at

nanotube mouth strongly affects the conductance by increasing the local concentration of counter-ions near the nanotube entrance.

Table 4.1 Values obtained from the best fit of conductance-concentration data in Fig. 4.5.a according to equations (4.1) to (4.3).

Electrolyte	G_{molar}	r (nm)	q (ē)	Adj. R-Square
LiCl	14.8 ± 3.5	0.39 ± 0.06	2.3 ± 0.4	0.98707
NaCl	34.4 ± 1.4	0.53 ± 0.02	3.0 ± 0.1	0.99891
KCl	67.9 ± 7.0	0.48 ± 0.05	2.5 ± 0.3	0.99587

There are several important considerations in using this model [166]. Firstly, the number of point charges, q, is not quite certain and can vary by a factor of two depending on whether the Debye-Hückel theory or the Nelson and McQuarrie treatment is considered. Second, certain factors (e.g. steric effects, interaction between adjacent carboxyl groups and variations in pK_a values) may lead to a disparity between the number of effective elementary charges obtained from the fitted data and the actual number of carboxylate groups present at the channel mouth. Another consideration is that, according to equation (4.2), anion concentration near the pore mouth is lower than the bulk phase. As a result, this conduction model ignores the anion contribution to ionic current, which is a reasonable assumption so long as the channel is highly cation selective. Lastly, any model that does not consider all the primary factors influencing the ion permeation in nanopores cannot completely elucidate the underlying physics of the process. Despite its simplicity, this model describes the general features and behaviors of the system fairly well and can serve as a foundation for the build-up of more comprehensive models in the future.

4.4.3 Conductance dependence on cation valency

We subjected the proposed model to another experiment. If the negatively charged carboxyl groups at the CNT entrance determine ion conduction as we hypothesized, the conductance and surface potential should be dependent on the valence of the screening ion but not on its type [86]. This is an effective way to examine the role of local surface charges on ion permeation in protein ion channel research. Divalent cations often cause a conductance reduction in biological pores by blocking the passage of more permeable ions [173] or by modulating the surface potentials through binding or charge screening [87, 174].

The shape and position of dose-response curves of divalent cations on conductance (i.e. conductance modulation, as divalent cation concentration is symmetrically increased across the channel) can in theory differentiate between these cases [86]. If divalent cations block the channel, flicker events are often observed; conductance approaches zero as divalent ion concentration becomes sufficiently high. The conductance decline will be dependent on the type of divalent ion. If divalent ions bind to the pore's charged functionalities, the dose-response curve will still depend on the chemical identity of the divalent cation but will level off at some non-zero conductance value. In the pure charge-screening scenario, the conductance will level off at some non-zero value, but the drop will be independent of the type of divalent species.

We measured the conductance of 200 mM KCl solution, at varying concentrations of added $MgCl_2$, $CaCl_2$, $SrCl_2$ or $BaCl_2$. Figure 4.6.a shows the normalized conductance with respect to the divalent free solution as a function of the divalent salt concentration over the same range. Upon the addition of divalent cations conductance not only does not rise, but rather sharply declines and eventually levels off at some non-zero value. This reduction in ionic conductance with the addition of divalent cations results from the electrostatic screening of surface charges, as is illustrated in Fig. 4.6.c. Divalent cations screen the surface charges to a much larger extent versus a similar concentration of monovalent cations (see equation (4.2)) [86, 171]. The reduction of conductance in Fig. 4.6.a is also independent of the nature of divalent species, indicating that divalent cations neither block the CNT pore nor bind to the carboxyl groups; they simply screen the surface charges at the pore mouth. These results further verify the proposed electrostatic mechanism for explaining ion conduction through narrow CNTs. Protein ion channels with fixed charges at the mouth, such as CaK channels produce similar results and conclusions if subjected to a similar experiment [87].

The results obtained from a leakage device are presented in Fig. 4.6.b. The conductance shows an increase in value upon addition of divalent cations to the solution.

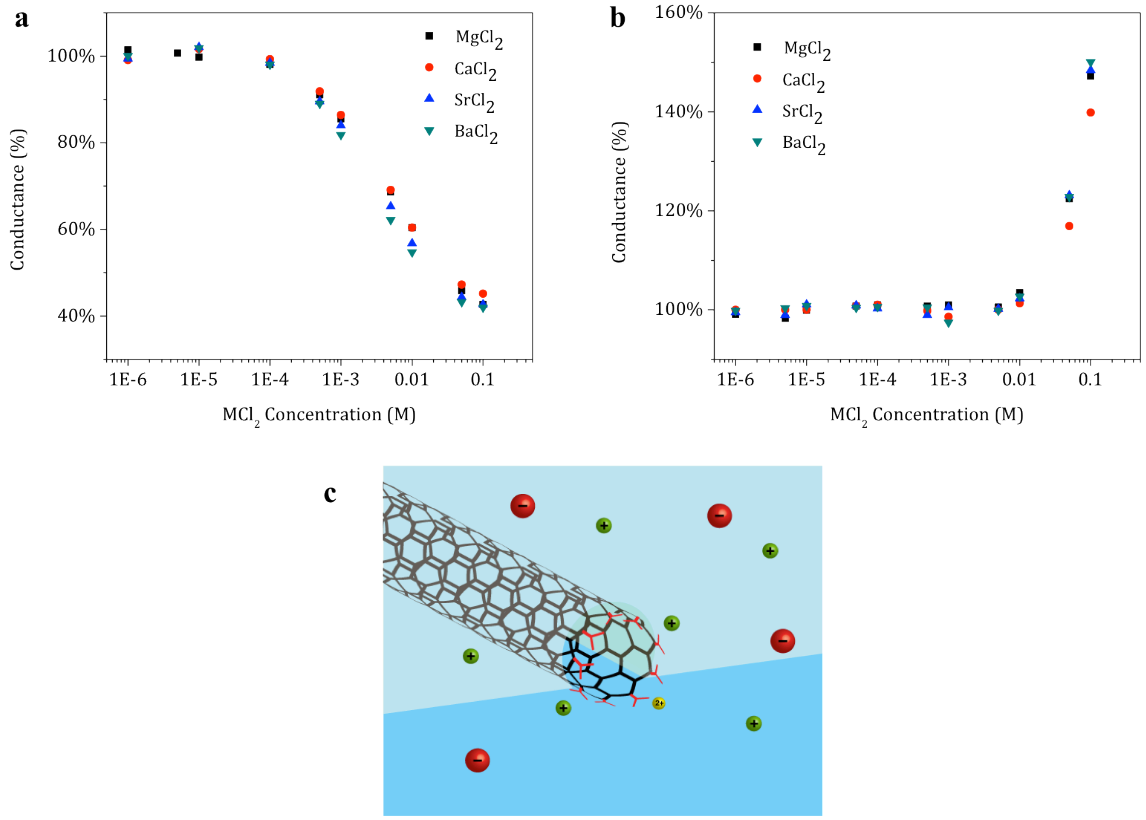

Figure 4.6 Effect of cation valency on conductance. Conductance variation, with respect to the divalent free solution, recorded as we symmetrically added divalent cations, $MgCl_2$ (black squares), $CaCl_2$ (red circles), $SrCl_2$ (blue triangles) and $BaCl_2$ (green triangles), to 200 mM KCl to give the desired M^{2+} concentration. a) CNT device. b) Leakage device. c) Cartoon representation of effective screening of negative surface charges at the nanotube mouth by divalent cations.

4.4.4 Conductance inhibition at high ion concentrations

In most solid-state nanopores, the ionic conductance-concentration curve at low ionic strengths is highly affected by surface charges on the pore; however, it tends to become linear again at sufficiently high concentrations as the surface electrostatics are effectively screened [149, 175]. Importantly, ionic conductance-concentration data obtained from CNT devices show a very different profile (Fig. 4.7). As the concentration of monovalent ions is raised equally in both solutions, conductance increases to a maximum value and then begins a descending phase. This behavior is similar to that observed in multi-ion protein channels [59].

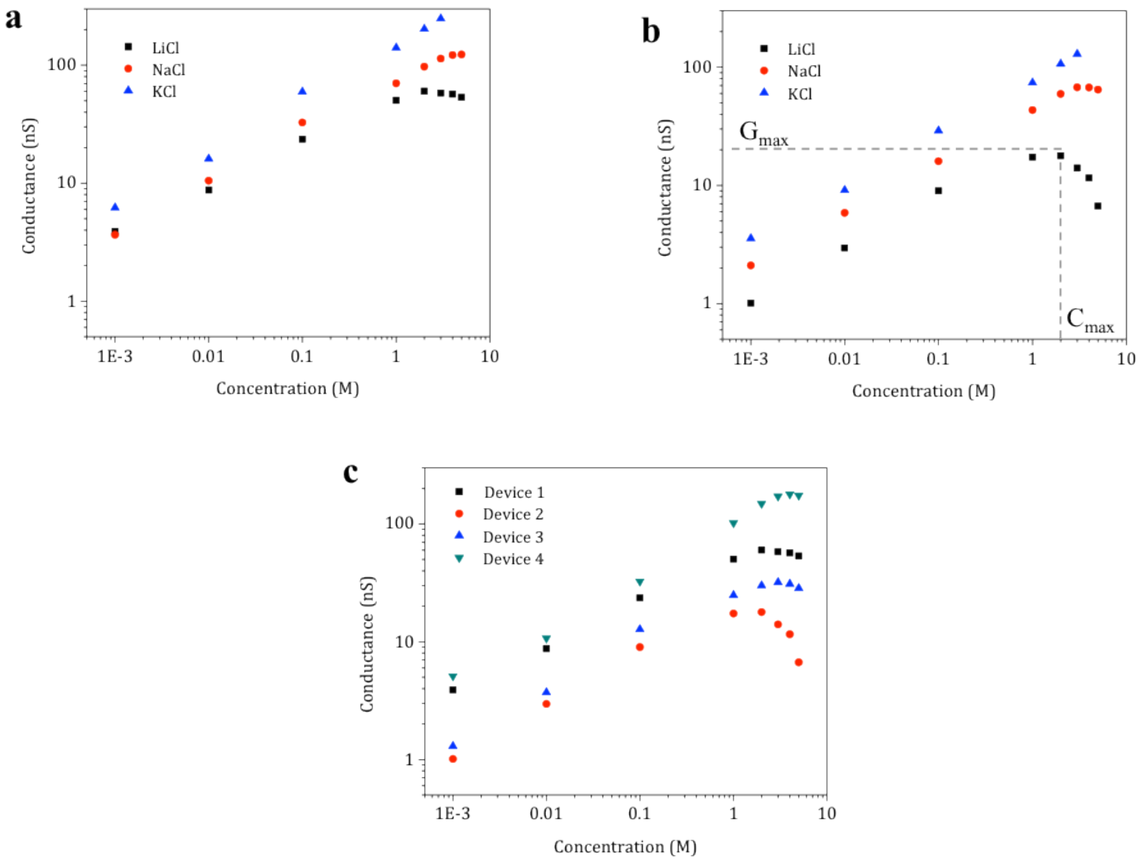

Figure 4.7 Conductance reduction at high ionic concentrations. a, b) Conductance-concentration profiles recorded from two different CNT devices in symmetrical solutions of LiCl, NaCl and KCl. c) Conductance-concentration profile recorded from four different CNT devices in symmetrical solutions of LiCl.

Certain protein channels can accommodate multiple ions in a queue within their permeation pathway; several ions move simultaneously in a single file fashion as each ion propels the one ahead of it [59]. The mutual repulsions between ions enforce a correlation in ion motions and prevent them from passing one another, even if they are small enough in size [176]. A remarkable example of mutual repulsions in the natural pores is calcium channels in frog muscle, where Ca^{2+} ions exit the pore 20,000 times faster when a second ion is entering the pore [177]. In multi-ion channels, since ions pass through pores which may already contain other ions, the number of ions present in the queue (i.e. multiple states of channel occupancy) becomes a function of solution concentrations, energy barrier heights, and the electric potentials across the channel [176].

It is often observed experimentally that the conductance of multi-ion pores reaches a maximum value and then starts a descending phase as the concentration of permeant ion is raised to sufficiently high levels on both sides of the membrane [59]. Several research groups have worked on building kinetics-based models to explain the conductance-concentration dependence in multi-ion channels [176, 178, 179]. One model used to explain the conductance reduction in biological channels proposes that ions need vacancies inside the channel to move into in order to maintain the flux [176]. At high ion concentrations the channel is saturated with ions and as one ion exits the pore into the solution and leaves behind a vacancy for its following ions to move into, another ion from the same solution jumps back into the pore and fills it up. In channels with multi-ion occupancy, such as CaK and Gramicidin A, conductance inhibition at sufficiently high ion concentrations is typically observed [141, 180].

Conductance-concentration profiles of CNTs also exhibit a descending phase at high concentrations (≥ 2.0 M), which can be explained through the same multi-ion conduction mechanism. Figures 4.7.a and 4.7.b show the changes in ionic conductance as the concentration of LiCl, NaCl or KCl electrolyte is varied over a large range in each of the two CNT devices with different conductivity levels. Figure 4.7.c compares the LiCl conductance-concentration graphs measured in four different CNT devices. In a single device, the electrolyte with the lower conductivity level always appears to exhibit a conductance maximum, G_{max}, at a lower concentration, C_{max} (Fig. 4.7.a and 4.7.b). A similar relationship between G_{max} and C_{max} is observed for one electrolyte type across different devices (Fig. 4.7.c). Conductance inhibition occurs when the channel is saturated, exactly as in the protein ion channel case. Less conductive channels/electrolytes often reach saturation at lower and more experimentally accessible concentrations [181]. For instance, a conductance maximum is not observed with CaK channels in up to 2.0 M of K^+; however, it is detected when less conductive Rb^+ is used instead [120, 180].

The concerted movement of ions along SWCNTs in a single-file fashion enforced by mutual repulsions has been reported by MD simulation studies [84, 182]. For instance, H. Liu et al. studied the transport of aqueous NaCl solution through SWCNTs (2.36 nm in length and ~ 0.9 nm in internal diameter in the absence of an external electric field and surface charges) by means of MD simulations and observed single-file concerted movement of ions along the nanopore [84]. In their simulations, co-ions have never been seen to be passing each other inside the pore, as intrinsic repulsion kept them separated. However, ions of opposite charge did pass each other; this suggests that this type of ion movement is not exclusive to multi-ion biological ion channels, but is most likely related to the transport of hydrated ions through hydrophobic nanotubes. The H. Liu et al. study also demonstrate that electrostatic repulsive forces between ions impacted their rate of progress in the tube, meaning that the first ion in the pore moved further along in a concerted multi-ion manner upon entry of second co-ion into the pore. Cooperative movement of K^+ cations was also observed in a concerted and accelerated fashion in the MD simulations study T. Sumikama et al. performed on an anion-doped CNT nanopore; their data further supports the significance of ion-ion repulsions on ion conduction process through narrow CNTs [182].

Some biological multi-ion channels exhibit a minimum (or a maximum) in single-channel conductance when the mole fraction of two electrolytes in solution is varied at constant total ion concentration [59, 183]. This behavior is so-called “anomalous mole-fraction effect”. Figure 4.8.a shows the anomalous mole-fraction effect in the zero-voltage conductance of CaK channel recorded in different compositions of K^+ and NH_4^+ [120]. As the mole fraction of K^+ is increased in the mixture, channel conductance goes through a minimum.

We performed similar measurements on our CNT devices in the mixture of KCl and LiCl with total ion concentrations of 30 mM or 3.0 M (Fig. 4.8.b). Anomalous mole-fraction effect was not apparent in any of the CNT devices tested.

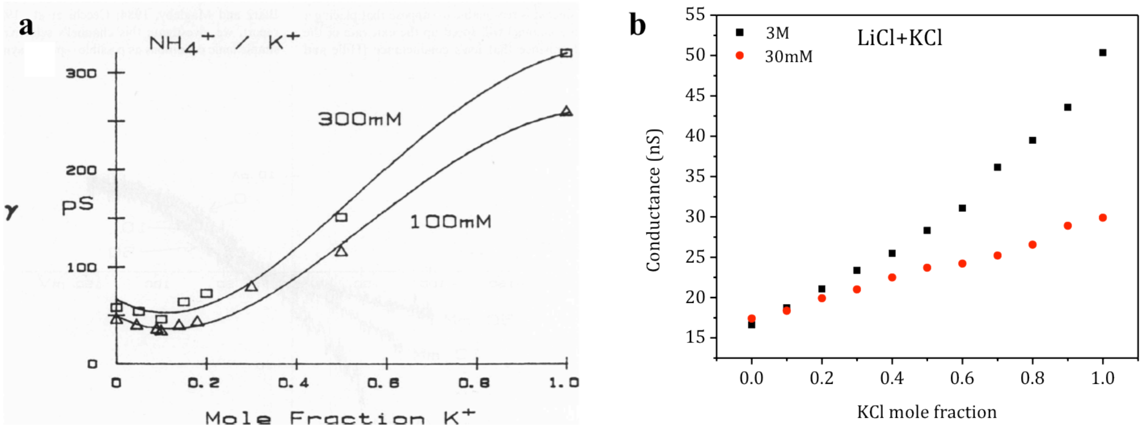

Figure 4.8 Anomalous mole-fraction effect. a) Zero voltage conductance measured in CaK channels facing symmetrical solutions of varying mixtures of K^+ and NH_4^+. Adapted in part from ref. [120]. b) Conductance of a CNT device in mixtures of LiCl and KCl with varying composition, total salt concentration was either 30 mM (red circles) or 3.0 M (black squares). No apparent anomalous mole-fraction behavior was observed in CNT-devices.

Another potential justification for conductance reduction at high concentrations can be related to J. Wu et al.'s proposal to explain the electrophoretic mobility drop of K^+ as the salt concentration was increased across a carbon nanotube membrane [34]. They suggested that at high concentrations, the surface charges are effectively screened allowing the entry of anions into the nanotube. This should reduce the electroosmotic current generated by the excess cation concentration inside the channel. It is likely that the conductance reduction is caused by the variations in ionic activity at high electrolyte concentrations because the control experiments we performed on leaky devices without CNTs have never demonstrated this type of behavior (Fig. 3.6.b).

Although the origin of the descending phase of conductance in our narrow CNT devices is not readily apparent, it points towards the ion-ion interactions inside the pore. It also stresses the fact that free energy profile calculations based on a single ion may not necessarily provide a full picture of the underlying mechanism of ion permeation.

CHAPTER 5

Conclusion and Outlook

5.1 Summary

In conclusion, this dissertation presents the result of a series of experiments designed to unravel the ion transport mechanisms in small diameter carbon nanotubes, specially, ≤ 1.5 nm in diameter and 20 μm in length. At this length scale the behavior of fluids and factors governing the transport begin to deviate from continuum descriptions of fluidic dynamics, as the molecular nature and complex interplay among channel, water and ions become significantly important. Small diameter carbon nanotubes hold a great potential for nanofluidic-based applications including single molecular analysis and sensing, analyte separation and water desalination. Although the number of computational studies on underlying physics of electrolyte transport through carbon nanotubes has rapidly grown over the past few years, experimental data has remained sparse, especially at the single nanotube level.

We hypothesized that the negative electrostatic potential arising from the deprotonated carboxyl groups at the carbon nanotube entrance play an important role in determining the channel's ion selectivity and conductance. We examined this hypothesis by studying the effect of electrolyte properties and pore surface charge modulation on ionic conductance and reversal potential.

Our single nanotube devices exhibit high selectivity towards cations over anions. Reversal potential measurements allow us to quantify the permeability ratio of cations over anions using Goldman-Hodgkin-Katz formulation [134, 135]. We provide experimental evidence suggesting that ions' hydration complex undergoes an energetically costly transformation as they translocate through small diameter nanotubes. This phenomenon has been demonstrated by several molecular dynamics simulation studies. We showed this effect by comparing the permeability of K^+-like ions, which have comparable bare radii, hydrated radii and bulk mobilities, at various concentrations. The cations with looser water molecules in their hydration shells (smaller enthalpy of hydration) exhibited higher conductance values. The presence of free energy barriers to ion permeation seems to explain the conductance saturation at high ionic concentrations. The non-monotonic trend of channel conductance in equally concentrated solutions of alkali metal chloride series highlights the complex nature of the ion permeation process through confined interior of carbon nanotubes and the necessity of further experimental and theoretical studies.

We established the location and nature of pore surface charges by studying the effect of surface charge modulation (i.e. through electrolyte screening, electrostatic adsorption of polycation chains and pH variations) on conductance and reversal potential. We then rationalize the experimental results by using a model, drawn from previous literature on protein ion channels. This model is built on a simplified version of the Gouy-Chapman theory of electrical double layer.

Carbon nanotubes are structural analogues of biological nanochannels, which make them promising candidates for the development of artificial biomimetic nanopores able to reproduce some of the most critical biological ion channel properties. In addition to the fundamental aspect of this study, this dissertation attempts to demonstrate the general similarities in ion permeation characteristics between carbon nanotubes and biological nanochannels.

5.2 Future direction

Given our robust measurement platform based on a single carbon nanotube and what we have learned so far on ion transport, I see a great potential for the project to grow in many different exciting directions. Here I mention a few:

It has been observed experimentally that metallic CNTs exhibit higher ionic conductances than semiconducting CNTs [41, 42]. However, there remains no compelling rationalization for this observation. Raman spectroscopy can add an additional characterization dimension to determine the type, chirality and inner diameter of the nanotubes [184]. A systematic study with well-characterized CNTs can help us to better understand the origin of higher conductance in metallic nanotubes.

Another unexplored area is the effect of nanotube length on its ion transport characteristics. Unraveling the relationship between nanotube length and its ionic conductance would add a valuable piece of data to better understand its conduction mechanism. Fortunately, the CVD-grown CNTs are long enough to permit the fabrication of several devices out of the same tube.

One of the important consequences of confining water and other molecules in nano-sized geometries is the formation of ordered structures [35, 127]. Carbon nanotubes provide a valuable template to study the effects of confinement on fluid behavior. Experiments can be designed to study the effect of fluid properties (e.g. viscosity, hydrogen bond forming ability etc.) on the transport by using different solvents/mixtures or adding molecules such as ionic liquid crystals to the solutions.

Aside from water and ions, small organic molecules and DNA strands can also translocate through carbon nanotubes with diameters as small as ~ 2 nm [41, 42]. It has been shown that the translocation of small single-stranded DNA molecules manifests as large spikes in ionic current. However, there many questions left to answer with regard to spikes origin and characteristics. Experiments designed using DNAs with various lengths or structural modifications can help us gain insight into DNA translocation through these channels.

So far our measurement set-up only allows us to extract information from the conductance and reversal potential data. Optical microscopy can provide an additional valuable tool to study these systems [185]. As explained in section 2.2.1.3 we were able to transfer CNTs onto glass coverslips with a satisfactory level of cleanness essential for TIRF microscopy. The similar fabrication procedure can be used to fabricate comparable nanofluidic devices out of transferred CNTs on a glass coverslip. The thin excitation field of an objective-based TIRF may allow us to study fluorescently tagged molecules in these type of devices without a large background noise.

Bibliography

1. Daiguji, H., *Ion transport in nanofluidic channels.* Chemical Society Reviews, 2010. **39**(3): p. 901-911.

2. Abgrall, P. and N.T. Nguyen, *Nanofluidic devices and their applications.* Analytical Chemistry, 2008. **80**(7): p. 2326-2341.

3. Venkatesan, B.M. and R. Bashir, *Nanopore sensors for nucleic acid analysis.* Nature Nanotechnology, 2011. **6**(10): p. 615-624.

4. Nakane, J.J., M. Akeson, and A. Marziali, *Nanopore sensors for nucleic acid analysis.* Journal of Physics-Condensed Matter, 2003. **15**(32): p. R1365-R1393.

5. Wanunu, M., *Nanopores: A journey towards DNA sequencing.* Physics of Life Reviews, 2012. **9**(2): p. 125-158.

6. Kasianowicz, J.J., et al., *Characterization of individual polynucleotide molecules using a membrane channel.* Proceedings of the National Academy of Sciences of the United States of America, 1996. **93**(24): p. 13770-13773.

7. Branton, D., et al., *The potential and challenges of nanopore sequencing.* Nature Biotechnology, 2008. **26**(10): p. 1146-1153.

8. Li, J., et al., *Ion-beam sculpting at nanometre length scales.* Nature, 2001. **412**(6843): p. 166-169.

9. Clarke, J., et al., *Continuous base identification for single-molecule nanopore DNA sequencing.* Nature Nanotechnology, 2009. **4**(4): p. 265-270.

10. Doyle, D.A., et al., *The structure of the potassium channel: Molecular basis of K+ conduction and selectivity.* Science, 1998. **280**(5360): p. 69-77.

11. Song, L.Z., et al., *Structure of staphylococcal alpha-hemolysin, a heptameric transmembrane pore.* Science, 1996. **274**(5294): p. 1859-1866.

12. Nguyen, T.L., *Three-dimensional model of the pore form of anthrax protective antigen. Structure and biological implications.* Journal of Biomolecular Structure & Dynamics, 2004. **22**(3): p. 253-265.

13. Kim, M.J., et al., *Rapid fabrication of uniformly sized nanopores and nanopore arrays for parallel DNA analysis.* Advanced Materials, 2006. **18**(23): p. 3149-+.

14. Ito, T., L. Sun, and R.M. Crooks, *Simultaneous determination of the size and surface charge of individual nanoparticles using a carbon nanotube-based coulter counter.* Analytical Chemistry, 2003. **75**(10): p. 2399-2406.

15. Li, N.C., et al., *Conical nanopore membranes. Preparation and transport properties.* Analytical Chemistry, 2004. **76**(7): p. 2025-2030.

16. Kasianowicz, J.J., et al., *Nanoscopic Porous Sensors.* Annual Review of Analytical Chemistry, 2008. **1**: p. 737-766.

17. Zwolak, M. and M. Di Ventra, *Electronic signature of DNA nucleotides via transverse transport.* Nano Letters, 2005. **5**(3): p. 421-424.

18. Gracheva, M.E., et al., *Simulation of the electric response of DNA translocation through a semiconductor nanopore-capacitor.* Nanotechnology, 2006. **17**(3): p. 622-633.

19. Haque, F., et al., *Solid-state and biological nanopore for real-time sensing of single chemical and sequencing of DNA.* Nano Today, 2013. **8**(1): p. 56-74.

20. Dekker, C., *Solid-state nanopores.* Nature Nanotechnology, 2007. **2**(4): p. 209-215.

21. Venta, K., et al., *Differentiation of Short, Single-Stranded DNA Homopolymers in Solid-State Nanopores.* Acs Nano, 2013. **7**(5): p. 4629-4636.

22. Schrlau, M.G., et al., *Carbon nanopipettes characterize calcium release pathways in breast cancer cells.* Nanotechnology, 2008. **19**(32).

23. Lee, S.B., et al., *Antibody-based bio-nanotube membranes for enantiomeric drug separations.* Science, 2002. **296**(5576): p. 2198-2200.

24. Fornasiero, F., et al., *Ion exclusion by sub-2-nm carbon nanotube pores.* Proceedings of the National Academy of Sciences of the United States of America, 2008. **105**(45): p. 17250-17255.

25. Daiguji, H., et al., *Theoretical study on the efficiency of nanofluidic batteries.* Electrochemistry Communications, 2006. **8**(11): p. 1796-1800.

26. Schoch, R.B., J.Y. Han, and P. Renaud, *Transport phenomena in nanofluidics.* Reviews of Modern Physics, 2008. **80**(3): p. 839-883.

27. Schmid, G., *Electrochemistry of capillary systems with narrow pores. II. Electroosmosis.* Journal of Membrane Science, 1998. **150**(2): p. 159-170.

28. Fornasiero, F., et al., *pH-Tunable Ion Selectivity in Carbon Nanotube Pores.* Langmuir, 2010. **26**(18): p. 14848-14853.

29. Sun, L. and R.M. Crooks, *Single carbon nanotube membranes: A well-defined model for studying mass transport through nanoporous materials.* Journal of the American Chemical Society, 2000. **122**(49): p. 12340-12345.

30. See, C.H. and A.T. Harris, *A review of carbon nanotube synthesis via fluidized-bed chemical vapor deposition.* Industrial & Engineering Chemistry Research, 2007. **46**(4): p. 997-1012.

31. Jin, Z., et al., *Ultralow feeding gas flow guiding growth of large-scale horizontally aligned single-walled carbon nanotube arrays.* Nano Letters, 2007. **7**(7): p. 2073-2079.

32. Bianco, A., et al., *Biomedical Applications of Functionalised Carbon Nanotubes.* Medicinal Chemistry and Pharmacological Potential of Fullerenes and Carbon Nanotubes, 2008. **1**: p. 23-+.

33. Miller, S.A., V.Y. Young, and C.R. Martin, *Electroosmotic flow in template-prepared carbon nanotube membranes.* Journal of the American Chemical Society, 2001. **123**(49): p. 12335-12342.

34. Wu, J., et al., *Electrophoretically induced aqueous flow through single-walled carbon nanotube membranes.* Nature Nanotechnology, 2012. **7**(2): p. 133-139.

35. Hummer, G., J.C. Rasaiah, and J.P. Noworyta, *Water conduction through the hydrophobic channel of a carbon nanotube.* Nature, 2001. **414**(6860): p. 188-190.

36. Majumder, M., N. Chopra, and B.J. Hinds, *Mass Transport through Carbon Nanotube Membranes in Three Different Regimes: Ionic Diffusion and Gas and Liquid Flow.* Acs Nano, 2011. **5**(5): p. 3867-3877.

37. Majumder, M., N. Chopra, and B.J. Hinds, *Effect of tip functionalization on transport through vertically oriented carbon nanotube membranes.* Journal of the American Chemical Society, 2005. **127**(25): p. 9062-9070.

38. Majumder, M., et al., *Voltage gated carbon nanotube membranes.* Langmuir, 2007. **23**(16): p. 8624-8631.

39. Hinds, B.J., et al., *Aligned multiwalled carbon nanotube membranes.* Science, 2004. **303**(5654): p. 62-65.

40. Holt, J.K., et al., *Fast mass transport through sub-2-nanometer carbon nanotubes.* Science, 2006. **312**(5776): p. 1034-1037.

41. Liu, H.T., et al., *Translocation of Single-Stranded DNA Through Single-Walled Carbon Nanotubes.* Science, 2010. **327**(5961): p. 64-67.

42. Liu, L., et al., *Ultrashort single-walled carbon nanotubes in a lipid bilayer as a new nanopore sensor.* Nature Communications, 2013. **4**.

43. Corredor, C., et al., *Disruption of model cell membranes by carbon nanotubes.* Carbon, 2013. **60**: p. 67-75.

44. Singh, R., et al., *Tissue biodistribution and blood clearance rates of intravenously administered carbon nanotube radiotracers.* Proceedings of the National Academy of Sciences of the United States of America, 2006. **103**(9): p. 3357-3362.

45. Hilder, T.A., D. Gordon, and S.H. Chung, *Synthetic Chloride-Selective Carbon Nanotubes Examined by Using Molecular and Stochastic Dynamics.* Biophysical Journal, 2010. **99**(6): p. 1734-1742.

46. Naguib, N., et al., *Observation of water confined in nanometer channels of closed carbon nanotubes.* Nano Letters, 2004. **4**(11): p. 2237-2243.

47. Byl, O., et al., *Unusual hydrogen bonding in water-filled carbon nanotubes.* Journal of the American Chemical Society, 2006. **128**(37): p. 12090-12097.

48. Maniwa, Y., et al., *Water-filled single-wall carbon nanotubes as molecular nanovalves.* Nature Materials, 2007. **6**(2): p. 135-141.

49. Wei, C.Y. and D. Srivastava, *Theory of transport of long polymer molecules through carbon nanotube channels.* Physical Review Letters, 2003. **91**(23).

50. Xie, Y.H., et al., *Electric field-induced translocation of single-stranded DNA through a polarized carbon nanotube membrane.* Journal of Chemical Physics, 2007. **127**(22).

51. Yeh, I.C. and G. Hummer, *Nucleic acid transport through carbon nanotube membranes.* Proceedings of the National Academy of Sciences of the United States of America, 2004. **101**(33): p. 12177-12182.

52. Kalman, E.B., et al., *Control of ionic transport through gated single conical nanopores.* Analytical and Bioanalytical Chemistry, 2009. **394**(2): p. 413-419.

53. He, Y.H., et al., *Controlling DNA Translocation through Gate Modulation of Nanopore Wall Surface Charges.* Acs Nano, 2011. **5**(7): p. 5509-5518.

54. Rincon-Restrepo, M., et al., *Controlled Translocation of Individual DNA Molecules through Protein Nanopores with Engineered Molecular Brakes.* Nano Letters, 2011. **11**(2): p. 746-750.

55. Sinha, S., et al., *Induction and measurement of minute flow rates through nanopipes.* Physics of Fluids, 2007. **19**(1).

56. Lee, C.Y., et al., *Coherence Resonance in a Single-Walled Carbon Nanotube Ion Channel.* Science, 2010. **329**(5997): p. 1320-1324.

57. Choi, W., et al., *Diameter-dependent ion transport through the interior of isolated single-walled carbon nanotubes.* Nature Communications, 2013. **4**.

58. Choi, W., et al., *Dynamics of Simultaneous, Single Ion Transport through Two Single-Walled Carbon Nanotubes: Observation of a Three-State System.* Journal of the American Chemical Society, 2011. **133**(2): p. 203-205.

59. Hille, B., *Ion channels of excitable membranes*. 3rd ed2001, Sunderland, Mass.: Sinauer. xviii, 814 p.

60. Jentsch, T.J., C.A. Hubner, and J.C. Fuhrmann, *Ion channels: Function unravelled by dysfunction.* Nature Cell Biology, 2004. **6**(11): p. 1039-1047.

61. Cooper, E.C. and L.Y. Jan, *Ion channel genes and human neurological disease: recent progress, prospects, and challenges.* Proc Natl Acad Sci U S A, 1999. **96**(9): p. 4759-66.

62. Dworakowska, B. and K. Dolowy, *Ion channels-related diseases.* Acta Biochimica Polonica, 2000. **47**(3): p. 685-703.

63. Proks, P. and J.D. Lippiat, *Membrane ion channels and diabetes.* Current Pharmaceutical Design, 2006. **12**(4): p. 485-501.

64. Kaczorowski, G.J., et al., *Ion channels as drug targets: The next GPCRs.* Journal of General Physiology, 2008. **131**(5): p. 399-405.

65. Bagal, S., et al., *Ion Channels as Therapeutic Targets: A Drug Discovery Perspective.* Journal of Medicinal Chemistry, 2013. **56**(3): p. 593-624.

66. Peter, C. and G. Hummer, *Ion transport through membrane-spanning nanopores studied by molecular dynamics simulations and continuum electrostatics calculations.* Biophysical Journal, 2005. **89**(4): p. 2222-2234.

67. Kowalczyk, S.W., T.R. Blosser, and C. Dekker, *Biomimetic nanopores: learning from and about nature.* Trends in Biotechnology, 2011. **29**(12): p. 607-614.

68. Pradeep, H. and G.K. Rajanikant, *Nanochannels: biological channel analogues.* Iet Nanobiotechnology, 2012. **6**(2): p. 63-70.

69. Hilder, T.A., D. Gordon, and S.H. Chung, *Boron nitride nanotubes selectively permeable to cations or anions.* Small, 2009. **5**(24): p. 2870-5.

70. Hou, X., et al., *A Biomimetic Potassium Responsive Nanochannel: G-Quadruplex DNA Conformational Switching in a Synthetic Nanopore.* Journal of the American Chemical Society, 2009. **131**(22): p. 7800-7805.

71. Tian, Y., et al., *A biomimetic zinc activated ion channel.* Chemical Communications, 2010. **46**(10): p. 1682-1684.

72. Yameen, B., et al., *Synthetic Proton-Gated Ion Channels via Single Solid-State Nanochannels Modified with Responsive Polymer Brushes.* Nano Letters, 2009. **9**(7): p. 2788-2793.

73. Caspi, Y., et al., *Synthetic Mimic of Selective Transport Through the Nuclear Pore Complex.* Nano Letters, 2008. **8**(11): p. 3728-3734.

74. Kowalczyk, S.W., et al., *Single-molecule transport across an individual biomimetic nuclear pore complex.* Nature Nanotechnology, 2011. **6**(7): p. 433-438.

75. Siwy, Z.S. and S. Howorka, *Engineered voltage-responsive nanopores.* Chemical Society Reviews, 2010. **39**(3): p. 1115-1132.

76. Majumder, M., A. Stinchcomb, and B.J. Hinds, *Towards mimicking natural protein channels with aligned carbon nanotube membranes for active drug delivery.* Life Sciences, 2010. **86**(15-16): p. 563-568.

77. Song, C. and B. Corry, *Intrinsic Ion Selectivity of Narrow Hydrophobic Pores.* Journal of Physical Chemistry B, 2009. **113**(21): p. 7642-7649.

78. Hilder, T.A., D. Gordon, and S.H. Chung, *Synthetic cation-selective nanotube: permeant cations chaperoned by anions.* Journal of Chemical Physics, 2011. **134**(4): p. 045103.

79. Joseph, S., et al., *Electrolytic transport in modified carbon nanotubes.* Nano Letters, 2003. **3**(10): p. 1399-1403.

80. Merdan, T., J. Kopecek, and T. Kissel, *Prospects for cationic polymers in gene and oligonucleotide therapy against cancer.* Advanced Drug Delivery Reviews, 2002. **54**(5): p. 715-758.

81. Garcia-Fandino, R. and M.S.P. Sansom, *Designing biomimetic pores based on carbon nanotubes.* Proceedings of the National Academy of Sciences of the United States of America, 2012. **109**(18): p. 6939-6944.

82. Hilder, T.A. and S.H. Chung, *Carbon nanotube as a gramicidin analogue.* Chemical Physics Letters, 2011. **501**(4-6): p. 423-426.

83. Zwolak, M., J. Wilson, and M. Di Ventra, *Dehydration and ionic conductance quantization in nanopores.* Journal of Physics-Condensed Matter, 2010. **22**(45).

84. Liu, H.M., S. Murad, and C.J. Jameson, *Ion permeation dynamics in carbon nanotubes.* Journal of Chemical Physics, 2006. **125**(8).

85. Gong, X., et al., *A controllable molecular sieve for Na+ and K+ ions.* Journal of the American Chemical Society, 2010. **132**(6): p. 1873-7.

86. Green, W.N. and O.S. Andersen, *Surface-Charges and Ion Channel Function.* Annual Review of Physiology, 1991. **53**: p. 341-359.

87. MacKinnon, R., R. Latorre, and C. Miller, *Role of surface electrostatics in the operation of a high-conductance Ca2+-activated K+ channel.* Biochemistry, 1989. **28**(20): p. 8092-9.

88. Iijima, S., *Helical Microtubules of Graphitic Carbon.* Nature, 1991. **354**(6348): p. 56-58.

89. Guo, T., et al., *Catalytic Growth of Single-Walled Nanotubes by Laser Vaporization.* Chemical Physics Letters, 1995. **243**(1-2): p. 49-54.

90. Joseyacaman, M., et al., *Catalytic Growth of Carbon Microtubules with Fullerene Structure.* Applied Physics Letters, 1993. **62**(2): p. 202-204.

91. Prasek, J., et al., *Methods for carbon nanotubes synthesis-review.* Journal of Materials Chemistry, 2011. **21**(40): p. 15872-15884.

92. Szabo, A., et al., *Synthesis Methods of Carbon Nanotubes and Related Materials.* Materials, 2010. **3**(5): p. 3092-3140.

93. Rastogi, R., et al., *Comparative study of carbon nanotube dispersion using surfactants.* Journal of Colloid and Interface Science, 2008. **328**(2): p. 421-428.

94. Stokes, P., et al., *Solution processed large area field effect transistors from dielectrophoreticly aligned arrays of carbon nanotubes.* Applied Physics Letters, 2009. **94**(11).

95. Bouchard, D., et al., *Aggregation Kinetics and Transport of Single-Walled Carbon Nanotubes at Low Surfactant Concentrations.* Environmental Science & Technology, 2012. **46**(8): p. 4458-4465.

96. Islam, M.F., et al., *High weight fraction surfactant solubilization of single-wall carbon nanotubes in water.* Nano Letters, 2003. **3**(2): p. 269-273.

97. Ibrahim, I., et al., *CVD-Grown Horizontally Aligned Single-Walled Carbon Nanotubes: Synthesis Routes and Growth Mechanisms.* Small, 2012. **8**(13): p. 1973-1992.

98. Kumar, M. and Y. Ando, *Chemical Vapor Deposition of Carbon Nanotubes: A Review on Growth Mechanism and Mass Production.* Journal of Nanoscience and Nanotechnology, 2010. **10**(6): p. 3739-3758.

99. Liu, J., S.S. Fan, and H.J. Dai, *Recent advances in methods of forming carbon nanotubes.* Mrs Bulletin, 2004. **29**(4): p. 244-250.

100. Li, Y.M., et al., *Growth of single-walled carbon nanotubes from discrete catalytic nanoparticles of various sizes.* Journal of Physical Chemistry B, 2001. **105**(46): p. 11424-11431.

101. Huang, L.M., et al., *Long and oriented single-walled carbon nanotubes grown by ethanol chemical vapor deposition.* Journal of Physical Chemistry B, 2004. **108**(42): p. 16451-16456.

102. Sfeir, M.Y., et al., *Optical spectroscopy of individual single-walled carbon nanotubes of defined chiral structure.* Science, 2006. **312**(5773): p. 554-556.

103. Jiao, L.Y., et al., *Creation of nanostructures with poly(methyl methacrylate)-mediated nanotransfer printing.* Journal of the American Chemical Society, 2008. **130**(38): p. 12612-+.

104. Manz, A., et al., *Design of an Open-Tubular Column Liquid Chromatograph Using Silicon Chip Technology.* Sensors and Actuators B-Chemical, 1990. **1**(1-6): p. 249-255.

105. Harrison, D.J., et al., *Capillary Electrophoresis and Sample Injection Systems Integrated on a Planar Glass Chip.* Analytical Chemistry, 1992. **64**(17): p. 1926-1932.

106. Ng, J.M.K., et al., *Components for integrated poly(dimethylsiloxane) microfluidic systems.* Electrophoresis, 2002. **23**(20): p. 3461-3473.

107. Becker, H. and L.E. Locascio, *Polymer microfluidic devices.* Talanta, 2002. **56**(2): p. 267-287.

108. Mao, H.B., T.L. Yang, and P.S. Cremer, *A microfluidic device with a linear temperature gradient for parallel and combinatorial measurements.* Journal of the American Chemical Society, 2002. **124**(16): p. 4432-4435.

109. Kopp, M.U., A.J. de Mello, and A. Manz, *Chemical amplification: Continuous-flow PCR on a chip.* Science, 1998. **280**(5366): p. 1046-1048.

110. Delamarche, E., et al., *Patterned delivery of immunoglobulins to surfaces using microfluidic networks.* Science, 1997. **276**(5313): p. 779-781.

111. Whitesides, G.M., et al., *Soft lithography in biology and biochemistry.* Annual Review of Biomedical Engineering, 2001. **3**: p. 335-373.

112. Kane, R.S., et al., *Patterning proteins and cells using soft lithography.* Biomaterials, 1999. **20**(23-24): p. 2363-2376.

113. Merkel, T.C., et al., *Gas sorption, diffusion, and permeation in poly(dimethylsiloxane).* Journal of Polymer Science Part B-Polymer Physics, 2000. **38**(3): p. 415-434.

114. Xia, Y.N. and G.M. Whitesides, *Soft lithography.* Annual Review of Materials Science, 1998. **28**: p. 153-184.

115. Friend, J. and L. Yeo, *Fabrication of microfluidic devices using polydimethylsiloxane.* Biomicrofluidics, 2010. **4**(2).

116. Campbell, D.J., et al., *Replication and compression of bulk and surface structures with polydimethylsiloxane elastomer.* Journal of Chemical Education, 1999. **76**(4): p. 537-541.

117. Zhou, J., et al., *Molecular dynamics study on ionic hydration.* Fluid Phase Equilibria, 2002. **194**: p. 257-270.

118. Richards, L.A., et al., *Quantifying barriers to monovalent anion transport in narrow non-polar pores.* Physical Chemistry Chemical Physics, 2012. **14**(33): p. 11633-11638.

119. Aqvist, J. and V. Luzhkov, *Ion permeation mechanism of the potassium channel.* Nature, 2000. **404**(6780): p. 881-4.

120. Eisenman, G., R. Latorre, and C. Miller, *Multi-ion conduction and selectivity in the high-conductance Ca++-activated K+ channel from skeletal muscle.* Biophysical Journal, 1986. **50**(6): p. 1025-34.

121. Cannon, J.J., et al., *Competitive Entry of Sodium and Potassium into Nanoscale Pores.* Journal of Physical Chemistry B, 2010. **114**(38): p. 12252-12256.

122. Sardroodi, J.J., et al., *The preferential permeation of ions across carbon and boron nitride nanotubes.* Chemical Physics, 2012. **403**: p. 105-112.

123. Corry, B., *Designing carbon nanotube membranes for efficient water desalination.* Journal of Physical Chemistry B, 2008. **112**(5): p. 1427-1434.

124. Zwolak, M., J. Lagerqvist, and M. Di Ventra, *Quantized Ionic Conductance in Nanopores.* Physical Review Letters, 2009. **103**(12).

125. Shao, Q., et al., *Anomalous Hydration Shell Order of Na+ and K+ inside Carbon Nanotubes.* Nano Letters, 2009. **9**(3): p. 989-994.

126. Shao, Q., et al., *Molecular simulation study of temperature effect on ionic hydration in carbon nanotubes.* Physical Chemistry Chemical Physics, 2008. **10**(14): p. 1896-1906.

127. He, Z.J., et al., *Ice-like Water Structure in Carbon Nanotube (8,8) Induces Cationic Hydration Enhancement.* Journal of Physical Chemistry C, 2013. **117**(21): p. 11412-11420.

128. Imoto, K., et al., *Rings of Negatively Charged Amino-Acids Determine the Acetylcholine-Receptor Channel Conductance.* Nature, 1988. **335**(6191): p. 645-648.

129. Xu, L., et al., *Two rings of negative charges in the cytosolic vestibule of type-1 ryanodine receptor modulate ion fluxes.* Biophysical Journal, 2006. **90**(2): p. 443-453.

130. Aubin, C.N.S. and P. Linsdell, *Positive charges at the intracellular mouth of the pore regulate anion conduction in the CFTR chloride channel.* Journal of General Physiology, 2006. **128**(5): p. 535-545.

131. Moorhouse, A.J., et al., *Single channel analysis of conductance and rectification in cation-selective, mutant glycine receptor channels.* Journal of General Physiology, 2002. **119**(5): p. 411-425.

132. Pang, P., et al., *Origin of Giant Ionic Currents in Carbon Nanotube Channels.* Acs Nano, 2011. **5**(9): p. 7277-7283.

133. Joseph, N.R., M.B. Engel, and H.R. Catchpole, *Chemical Potentials + Electrical Potentials in Biological Systems.* Nature, 1964. **203**(494): p. 931-&.

134. Goldman, D.E., *Potential, impedance, and rectification in membranes.* Journal of General Physiology, 1944. **27**(1): p. 37-60.

135. Hodgkin, A.L. and B. Katz, *The Effect of Sodium Ions on the Electrical Activity of the Giant Axon of the Squid.* Journal of Physiology-London, 1949. **108**(1): p. 37-77.

136. Hille, B., *Ion Channels of Excitable Membranes (3rd Edition).* 2001.

137. Nightingale, E.R., *Phenomenological Theory of Ion Solvation - Effective Radii of Hydrated Ions.* Journal of Physical Chemistry, 1959. **63**(9): p. 1381-1387.

138. Barry, P.H. and J.W. Lynch, *Liquid Junction Potentials and Small-Cell Effects in Patch-Clamp Analysis.* Journal of Membrane Biology, 1991. **121**(2): p. 101-117.

139. Smith, D.W., *Ionic Hydration Enthalpies.* Journal of Chemical Education, 1977. **54**(9): p. 540-542.

140. Tabcharani, J.A., P. Linsdell, and J.W. Hanrahan, *Halide permeation in wild-type and mutant cystic fibrosis transmembrane conductance regulator chloride channels.* Journal of General Physiology, 1997. **110**(4): p. 341-54.

141. Finkelstein, A. and O.S. Andersen, *The gramicidin A channel: a review of its permeability characteristics with special reference to the single-file aspect of transport.* J Membr Biol, 1981. **59**(3): p. 155-71.

142. O'mara, M., et al., *Homology model of the GABA(A) receptor examined using Brownian dynamics.* Biophysical Journal, 2005. **88**(5): p. 3286-3299.

143. Kral, P. and B.Y. Wang, *Material Drag Phenomena in Nanotubes.* Chemical Reviews, 2013. **113**(5): p. 3372-3390.

144. Mead, F.C. and A.J. Williams, *Electrostatic mechanisms underlie neomycin block of the cardiac ryanodine receptor channel (RyR2).* Biophysical Journal, 2004. **87**(6): p. 3814-3825.

145. Scruggs, N.R., et al., *Rectification of the Ionic Current through Carbon Nanotubes by Electrostatic Assembly of Polyelectrolytes.* Nano Letters, 2009. **9**(11): p. 3853-3859.

146. Donnan, F.G., *The theory of membrane equilibria.* Chemical Reviews, 1924. **1**(1): p. 73-90.

147. Donnan, F.G., *Theory of Membrane Equilibria and Membrane-Potentials in the Presence of Non-Dialyzing Electrolytes - a Contribution to Physical-Chemical Physiology (Reprinted from Zeitshrift Fur Elektrochemie Und Angewandte Physikalische Chemie, Vol 17, Pg 572, 1911).* Journal of Membrane Science, 1995. **100**(1): p. 45-55.

148. Wong, S.S., et al., *Covalently functionalized nanotubes as nanometre-sized probes in chemistry and biology.* Nature, 1998. **394**(6688): p. 52-55.

149. Hoogerheide, D.P., S. Garaj, and J.A. Golovchenko, *Probing Surface Charge Fluctuations with Solid-State Nanopores.* Physical Review Letters, 2009. **102**(25).

150. Dukhin, A., S. Dukhin, and P. Goetz, *Electrokinetics at high ionic strength and hypothesis of the double layer with zero surface charge.* Langmuir, 2005. **21**(22): p. 9990-9997.

151. Kim, D. and E. Darve, *High-ionic-strength electroosmotic flows in uncharged hydrophobic nanochannels.* Journal of Colloid and Interface Science, 2009. **330**(1): p. 194-200.

152. Joseph, S. and N.R. Aluru, *Hierarchical multiscale simulation of electrokinetic transport in silica nanochannels at the point of zero charge.* Langmuir, 2006. **22**(21): p. 9041-9051.

153. Sparreboom, W., A. van den Berg, and J.C.T. Eijkel, *Transport in nanofluidic systems: a review of theory and applications.* New Journal of Physics, 2010. **12**.

154. Travis, K.P. and K.E. Gubbins, *Poiseuille flow of Lennard-Jones fluids in narrow slit pores.* Journal of Chemical Physics, 2000. **112**(4): p. 1984-1994.

155. Zhang, J.F., B.D. Todd, and K.P. Travis, *Viscosity of confined inhomogeneous nonequilibrium fluids.* Journal of Chemical Physics, 2004. **121**(21): p. 10778-10786.

156. Huang, C.K., et al., *Comparative study between continuum and atomistic approaches of liquid flow through a finite length cylindrical nanopore.* Journal of Chemical Physics, 2007. **126**(22).

157. Qiao, R. and N.R. Aluru, *Ion concentrations and velocity profiles in nanochannel electroosmotic flows.* Journal of Chemical Physics, 2003. **118**(10): p. 4692-4701.

158. Travis, K.P., B.D. Todd, and D.J. Evans, *Departure from Navier-Stokes hydrodynamics in confined liquids.* Physical Review E, 1997. **55**(4): p. 4288-4295.

159. Gracheva, M.E., *Nanopore-Based Technology*. Methods in molecular biology, methods and protocols2012, Totowa, NJ: Humana Press. Online-Ressource.

160. Shaw, D.E., et al., *Atomic-Level Characterization of the Structural Dynamics of Proteins.* Science, 2010. **330**(6002): p. 341-346.

161. Levitt, D.G., *Perspective - Modeling of ion channels.* Journal of General Physiology, 1999. **113**(6): p. 789-794.

162. Ingolfsson, H.I., et al., *Gramicidin A Backbone and Side Chain Dynamics Evaluated by Molecular Dynamics Simulations and Nuclear Magnetic Resonance Experiments. I: Molecular Dynamics Simulations.* Journal of Physical Chemistry B, 2011. **115**(22): p. 7417-7426.

163. Sakmann, B. and G. Trube, *Conductance Properties of Single Inwardly Rectifying Potassium Channels in Ventricular Cells from Guinea-Pig Heart.* Journal of Physiology-London, 1984. **347**(Feb): p. 641-&.

164. Benz, R., et al., *Pore Formation by the Escherichia-Coli Hemolysin - Evidence for an Association-Dissociation Equilibrium of the Pore-Forming Aggregates.* Infection and Immunity, 1989. **57**(3): p. 887-895.

165. Trias, J.Q. and R. Benz, *Characterization of the Channel Formed by the Mycobacterial Porin in Lipid Bilayer-Membranes - Demonstration of Voltage Gating and of Negative Point Charges at the Channel Mouth.* Journal of Biological Chemistry, 1993. **268**(9): p. 6234-6240.

166. Welte, W., et al., *X-ray crystallographic and mass spectrometric structure determination and functional characterisation of succinylated porin from Rhodobacter capsulatus: Implications for ion selectivity and single-channel conductance.* New Methods for the Study of Biomolecular Complexes, 1998. **510**: p. 239-276.

167. Benz, R., K.R. Hardie, and C. Hughes, *Pore Formation in Artificial Membranes by the Secreted Hemolysins of Proteus-Vulgaris and Morganella-Morganii.* European Journal of Biochemistry, 1994. **220**(2): p. 339-347.

168. Ropele, M. and G. Menestrina, *Electrical-Properties and Molecular Architecture of the Channel Formed by Escherichia-Coli Hemolysin in Planar Lipid-Membranes.* Biochimica Et Biophysica Acta, 1989. **985**(1): p. 9-18.

169. Menestrina, G. and R. Antolini, *Ion-Transport through Hemocyanin Channels in Oxidized Cholesterol Artificial Bilayer-Membranes.* Biochimica Et Biophysica Acta, 1981. **643**(3): p. 616-625.

170. Nelson, A.P. and D.A. McQuarrie, *The effect of discrete charges on the electrical properties of a membrane. I.* Journal of Theoretical Biology, 1975. **55**(1): p. 13-27.

171. Dani, J.A., *Ion-Channel Entrances Influence Permeation - Net Charge, Size, Shape, and Binding Considerations.* Biophysical Journal, 1986. **49**(3): p. 607-618.

172. Brunen, M., et al., *The Major Outer-Membrane Protein of Acidovorax-Delafieldii Is an Anion-Selective Porin.* Journal of Bacteriology, 1991. **173**(13): p. 4182-4187.

173. Arellano, R.O., R.M. Woodward, and R. Miledi, *A Monovalent Cationic Conductance That Is Blocked by Extracellular Divalent-Cations in Xenopus Oocytes.* Journal of Physiology-London, 1995. **484**(3): p. 593-604.

174. Hille, B., A.M. Woodhull, and B.I. Shapiro, *Negative surface charge near sodium channels of nerve: divalent ions, monovalent ions, and pH.* Philos Trans R Soc Lond B Biol Sci, 1975. **270**(908): p. 301-18.

175. Stein, D., M. Kruithof, and C. Dekker, *Surface-charge-governed ion transport in nanofluidic channels.* Physical Review Letters, 2004. **93**(3).

176. Hille, B. and W. Schwarz, *Potassium Channels as Multi-Ion Single-File Pores.* Journal of General Physiology, 1978. **72**(4): p. 409-442.

177. Almers, W. and E.W. McCleskey, *Non-selective conductance in calcium channels of frog muscle: calcium selectivity in a single-file pore.* J Physiol, 1984. **353**: p. 585-608.

178. Schumaker, M.F. and R. MacKinnon, *A simple model for multi-ion permeation. Single-vacancy conduction in a simple pore model.* Biophysical Journal, 1990. **58**(4): p. 975-84.

179. Kohler, H.H. and K. Heckmann, *Unidirectional Fluxes in Saturated Single-File Pores of Biological and Artificial Membranes .1. Pores Containing No More Than One Vacancy.* Journal of Theoretical Biology, 1979. **79**(3): p. 381-401.

180. A. Villarroel, A.a.G.E., *A maximum in conductance occurs for the large Ca-activated K channel at high Rb concentration.* Biophysical Journal, 1988. **53**: p. 259a.

181. Lu, Z. and R. MacKinnon, *A conductance maximum observed in an inward-rectifier potassium channel.* Journal of General Physiology, 1994. **104**(3): p. 477-86.

182. Sumikama, T., S. Saito, and I. Ohmine, *Mechanism of ion permeation in a model channel: Free energy surface and dynamics of K+ ion transport in an anion-doped carbon nanotube.* J Phys Chem B, 2006. **110**(41): p. 20671-7.

183. Nonner, W., D.P. Chen, and B. Eisenberg, *Anomalous mole fraction effect, electrostatics, and binding in ionic channels.* Biophysical Journal, 1998. **74**(5): p. 2327-2334.

184. Dresselhaus, M.S., G. Dresselhaus, and A. Jorio, *Raman spectroscopy of carbon nanotubes in 1997 and 2007.* Journal of Physical Chemistry C, 2007. **111**(48): p. 17887-17893.

185. Song, W.S., et al., *Optical and Electrical Detection of Single-Molecule Translocation through Carbon Nanotubes.* Acs Nano, 2013. **7**(1): p. 689-694.